PIKfyve influences inter-organelle contacts with lysosomes to modulate the endoplasmic reticulum

Nicala Jenkins[1,2], Zainab Adamji[1,2], Maria R. Narciso[1,2], Nourhan R. Almasri[1], Sharifa Lomiyev[1], and Roberto J. Botelho[1,2#]

[1]Department of Chemistry and Biology and [2]Molecular Science Graduate Program, Toronto Metropolitan University, Toronto, Ontario, M5B2K3, Canada

[#]To whom correspondence should be sent: rbotelho@torontomu.ca

Running title: PIKfyve and the endoplasmic reticulum

Keywords: Lipid kinases, organelles, lysosomes, ER, morphology, membrane contact sites

Summary: Long associated with the regulation of the endolysosomal pathway, the authors show that the PIKfyve lipid kinase extends its sphere of influence to modulate the architecture and dynamics of the endoplasmic reticulum by balancing phosphoinositide species at their inter-organellar sites.

23

24

25

26 **Abbreviations**

27 **Arl8b**: ADP-ribosylation factor like 8b; **Atg18:** autophagy-related protein 18; **ClC7:** chlorine
28 exchange transporter 7; **CLIMP63:** 63 kDa cytoskeleton linking protein; **EB1:** end-binding
29 protein 1; **ER:** endoplasmic reticulum; **FFAT**: two phenylalanine's (FF) in an acidic tract; **Fig4:**
30 factor-Induced gene 4; **FKBP:** FK506-binding protein; **FRB:** FKBP rapamycin binding; **FYCO1:**
31 FYVE and coiled-coil domain autophagy adaptor 1; **FYVE**: fab1, YOTB, Vac1 and EEA1 binding
32 domain; **FYVE4A:** fab1, YOTB, Vac1 and EEA1 binding domain mutant; **GFP:** green fluorescent
33 protein; **GST:** glutathione s-transferase; **GTPase**: guanine triphosphatase; KIF5B**:** kinesin-1
34 heavy chain isoform 5B; **LAMP1:** lysosomal associate membrane protein 1; **LCR:** low complexing
35 region; **mCherry/mCh:** monomeric cherry, red fluorescent protein; **MCS:** membrane contact
36 site; **mScarletI**: basic red fluorescent protein; **PI(3,5)P_2**:phosphatidylinositol 3,5-bisphosphate;
37 **PI(3)P**: phosphatidylinositol 3-phosphate; **PIKfyve**: phosphoinositide FYVE-type zinc finger
38 containing; **PIP**: phosphoinositide; **PtdIns:** phosphatidylinositol; **PLA:** proximity ligation assay;
39 **PX Domain:** phox homology domain; **Rab5:** ras-related protein-5; **Rab7:** ras-related protein-7;
40 **RFP:** red fluorescent protein; **RILP:** rab interacting lysosomal protein; **RILPC33**: rab interacting
41 lysosomal protein, c terminal 33aa fragment; **Rtn4a:** reticulon 4A; **RUFY3:** RUN and FYVE
42 domain containing 3; **RUFY4:** RUN and FYVE domain containing 4; **siRNA:** small interfering RNA;
43 **SnxA:** sorting nexin A; **Snx19:** sorting nexin 19; **TAC:** tip attachment complex; **TPC:** two pore
44 channel; **TRPML1:** transient receptor potential channel for mucolipin-1; **VAPA:** vesicle

associated membrane protein-associated protein A; **VAPB:** vesicle associated membrane protein-associated protein B; **VPS34:** vacuolar sorting protein 34; **VPS34 In1:** vacuolar sorting protein 34 inhibitor-1; **2XFYVE:** tandem FYVE domain.

Summary

Lysosomes clear unwanted cellular material delivered by constant membrane fusion. Membrane fission is thus required to balance lysosome size, number, and composition. PIKfyve is a lipid kinase that converts phosphatidylinositol-3-phosphate [PtdIns(3)P] to phosphatidylinositol-3,5-bisphosphate [PtdIns(3,5)P_2] and promotes lysosome fission since lysosomes coalesce into larger, but fewer organelles in its absence. Here, we reveal a role for PIKfyve in regulating endoplasmic reticulum (ER) dynamics. We show the ER is less reticulated and motile in cells inhibited for PIKfyve. Partly, this arises because lysosomes cluster perinuclearly and are less motile, which appears to arrest ER hitchhiking, a process in which lysosomes pull and form ER tubules. Secondly, the ER morphology is distorted because of hyper-tethering of protrudin, an ER transmembrane protein, to lysosomes via excess PtdIns(3)P and protrudin's FYVE domain. Our findings reveal that PIKfyve balances phosphoinositides at ER-lysosome contact sites to govern ER properties and have significant implications for our understanding of PIKfyve function and of diseases linked to its dysfunction.

67

68

69

70 **Introduction**

71 Lysosomes are acidic and degradative organelles that receive and digest a plethora of molecular
72 cargo from the endocytic, autophagic and phagocytic pathways (Ballabio and Bonifacino, 2020;
73 Inpanathan and Botelho, 2019). They are also highly dynamic because they continuously
74 undergo fusion-fission cycles with maturing late endosomes, transport vesicles from the *trans*-
75 Golgi network, and between themselves (Saffi and Botelho, 2019; Luzio et al., 2007). This
76 constant intermixing is dependent on bidirectional movement of lysosomes on microtubules
77 driven by kinesin and dynein motors (Cabukusta and Neefjes, 2018). Perhaps due to this
78 dynamic nature, lysosomes are a heterogeneous collection of organelles that differ in shape,
79 size, position, and function (Saffi and Botelho, 2019; Inpanathan and Botelho, 2019). Thus, and
80 unless otherwise indicated, we use the term *lysosomes* to encapsulate this full spectrum,
81 including late endosomes, terminal lysosomes, and their hybrids, endolysosomes.

82 Given this complexity, lysosomes are subject to various regulatory inputs including by
83 the Rab7 and Arl8b GTPases and the PIKfyve lipid kinase (Ballabio and Bonifacino, 2020; Bissig
84 et al., 2017; de Lartigue et al., 2009; Cantalupo et al., 2001; Khatter et al., 2015). PIKfyve is a
85 conserved lipid kinase that localizes to endosomes and lysosomes via its FYVE domain and
86 phosphatidylinositol-3-phosphate [PtdIns(3)P], which is then converted by PIKfyve into
87 phosphatidylinositol-3,5-bisphosphate [PtdIns(3,5)P_2] (Ikonomov et al., 2001; Sbrissa et al.,

88 2002, 2007). While deletion of PIKfyve is embryonic lethal, tissue-specific knockouts or
89 mutations that abate PtdIns(3,5)P_2 levels are associated with defects in immunity,
90 inflammation, metabolic, and neurological functions (Ikonomov et al., 2011; Min et al., 2014;
91 Chow et al., 2007; Tsuruta et al., 2009; Cheng et al., 2025; Min et al., 2019; Prado et al., 2025).
92 At the molecular level, there remain few known PtdIns(3,5)P_2-binding proteins, which include
93 Ca^{2+}, Cl^- and Na^+ channels like TRPML1, ClC7, and TPCs, respectively (Leray et al., 2022; Dong et
94 al., 2010; Wang et al., 2012), the actin regulator cortactin (Hong et al., 2015), and membrane
95 curvature factors like the yeast Atg18 (Gopaldass et al., 2017). Through these and other
96 unknown effectors, PIKfyve and PtdIns(3,5)P_2 collectively modulate osmosis, ion-based
97 signaling, lysosome fusion-fission cycling, and the degradative capacity of lysosomes (Bissig et
98 al., 2017; Choy et al., 2018; Leray et al., 2022; Dong et al., 2010; Sharma et al., 2019; Wang et
99 al., 2012). Arguably, the most conspicuous defect caused by PIKfyve loss of function is lysosome
100 enlargement and the concomitant decline in lysosome number, likely due to reduced
101 membrane fission relative to fusion (Bissig et al., 2017; Choy et al., 2018; Sharma et al., 2019).
102 However, we do not know if this occurs by dysregulation of fission complexes and/or of
103 signaling factors like ion-based signaling. Interestingly, endosomes and mitochondrial sites of
104 fission are demarcated by endoplasmic reticulum (ER)-dependent contacts (Friedman et al.,
105 2013; Abrisch et al., 2020; Friedman et al., 2011). We thus considered whether PIKfyve and the
106 ER may play a joint role in lysosome fission.

107 The ER is a reticulated membrane network composed of membrane sheets and tubules
108 extending throughout the cell, and forming functional domains such as the rough ER and
109 smooth ER (Westrate et al., 2015). The ER morphology is regulated by various proteins and

110 responds to signals such as the unfolded protein response and the nutrient status of the cell
111 (Chen et al., 2023; Goyal and Blackstone, 2013; Lu et al., 2020). For instance, ER sheets are
112 promoted by integral membrane proteins such as CLIMP63, which form bridge-like structures
113 connecting opposing ER bilayers (Shibata et al., 2010). In comparison, ER tubules are dynamic,
114 continually forming, branching, and rearranging through the action of proteins such as
115 Reticulons and Atlastins (Wang et al., 2016; Hu et al., 2009; Voeltz et al., 2006; Goyal and
116 Blackstone, 2013).

117 ER remodeling can also occur through motor and cytoskeleton-driven processes. This
118 includes microtubule tip attachment complex (TAC)-mediated movement and ER-sliding, which
119 rely on the interaction between the ER membrane and microtubules to facilitate the formation
120 of new ER tubules (Waterman-Storer and Salmon, 1998; Rodríguez-García et al., 2020; Spits et
121 al., 2021), and ER hitchhiking. During ER hitchhiking, the ER forms a contact with vesicles,
122 endosomes, or lysosomes (Guimaraes et al., 2015; Spits et al., 2021; Raiborg et al., 2015b; Lu et
123 al., 2020; Langley et al., 2025). The attached ER then co-migrates with the motile
124 endosome/lysosome in a motor and microtubule-dependent manner to grow a new ER tubule
125 (Guimaraes et al., 2015; Spits et al., 2021; Voeltz et al., 2024; Lu et al., 2020). Little is known
126 about the protein complexes holding the ER-endosome/lysosome together, but these are
127 thought to be maintained by tethering proteins such as protrudin (Raiborg et al., 2015b; a;
128 Pedersen et al., 2020; Spits et al., 2021).

129 Protrudin, which was originally identified as a protein that promotes neurite formation
130 (Shirane and Nakayama, 2006), is an ER-transmembrane protein that together with VAPA,

131 another ER transmembrane protein, and the lysosomal Rab7 GTPase, form an ER-lysosome
132 tethering complex (Raiborg et al., 2015a; Pedersen et al., 2020; Matsuzaki et al., 2011; Saita et
133 al., 2009). Protrudin has a FYVE domain and a protein-binding low complexing region (LCR) that
134 respectively are thought to bind to PtdIns(3)P and GTP-bound Rab7 on endosomes/lysosomes
135 (Raiborg et al., 2015a; Pedersen et al., 2020). Protrudin then extends its cytoplasmic region to
136 loop around and interact with VAPA via its FFAT motif. Through this contact, protrudin is
137 thought to load kinesin-1 onto lysosome-bound FYCO1, a Rab7 effector that promotes
138 lysosome anterograde movement and binds PtdIns(3)P (Pedersen et al., 2020; Raiborg et al.,
139 2015a; Jongsma et al., 2024; Matsuzaki et al., 2011; Pankiv et al., 2010). Collectively, protrudin
140 tethers ER-lysosomes together and modulates their relative dynamics (Cabukusta and Neefjes,
141 2018; Jongsma et al., 2016, 2024).

142 Overall, there is a bidirectional relationship between the ER and organelles of the endo-
143 lysosomal pathway through contact sites. ER contacts appear to define areas of endosome
144 fission, while endosomes and lysosomes help reshape the ER via hitchhiking. Given this, we
145 postulated that ER-driven fission may malfunction during PIKfyve inhibition, resulting in
146 lysosome coalescence. Additionally, we hypothesized that lysosome coalescence during PIKfyve
147 loss may alter ER morphology and dynamics. Here, we provide evidence that PIKfyve inhibition
148 potently distorts the ER morphology and dynamics by hindering ER hitchhiking and stabilizing
149 protrudin interaction with lysosomes via excess PtdIns(3)P levels.

150

151 **Results**

152 *Lysosome morphology is relatively intact in cells manipulated for ER morphology*

153 PIKfyve inhibition enlarges lysosomes via coalescence, ostensibly by perturbing fission (Choy et
154 al., 2018; Bissig et al., 2017; Sharma et al., 2019). On the other hand, sites of tubular endosome
155 fission are demarcated by ER tubules that wrap around endosomes (Friedman et al., 2013;
156 Rowland et al., 2014). Conceivably then, lysosome coalescence in PIKfyve-inhibited cells may be
157 the corollary of perturbed contacts between ER and endo-lysosomal structures. To test this
158 hypothesis, we over-expressed CLIMP63 or Rtn4A, which respectively bias ER towards sheets
159 and reticulated tubules (Shibata et al., 2010; Wang et al., 2016; Wu and Voeltz, 2021; Voeltz et
160 al., 2006), and examined their effect on the morphology and number of lysosomes labelled with
161 fluorescent dextrans in resting and apilimod-treated cells (Choy et al., 2018; Ohkuma and
162 Poole, 1978; Ferris et al., 1987).

163 As expected, COS-7 cells overexpressing mCh-CLIMP63 displayed an overwhelmingly
164 sheet-like ER network with a dramatic decline of ER tubules **(Fig. 1A).** Conversely, cells
165 expressing eGFP-Rtn4 had an exaggerated tubular ER network **(Fig 1B).** We then quantified the
166 total lysosome number and the individual lysosome volume in cells over-expressing CLIMP63 or
167 Rtn4 and treated with vehicle or apilimod to block PIKfyve. Remarkably, there was no
168 difference in lysosome size and number in cells expressing CLIMP63 or Rtn4 compared to the
169 respective mCherry or GFP controls **(Fig. 1C-F).** This shows that distortion of ER morphology
170 does not cause lysosome coalescence and does not mimic PIKfyve inactivation. Interestingly,
171 overexpression of CLIMP63 or Rtn4 respectively enhanced and reduced apilimod-driven
172 changes in the volume of individual lysosomes **(Fig. 1D, 1F),** but did not alter the total lysosome
173 number per cell (**Fig. 1C, 1E**). This suggests that the ER morphology can impact lysosome size,

174 but not by coalescence as in PIKfyve inactivation. Overall, these results show that manipulating
175 ER morphology does not readily mimic the effects of PIKfyve on lysosome dynamics but can
176 synergize with PIKfyve inactivation to influence lysosome size.
177
178 *PIKfyve inhibition distorts ER morphology*
179 We next considered the converse: whether lysosome distortion in PIKfyve-inhibited cells would
180 alter the ER morphology. To test this, we expressed ER-mNeonGreen in COS-7 cells to label the
181 ER and labelled lysosomes with a fluorescent dextran. We opted to first use a pharmacological
182 approach to block PIKfyve using apilimod or YM-201636 because this permitted acute
183 disturbance of lysosomes, mitigating indirect effects on the ER.
184 In vehicle-treated cells, the ER network exhibited a series of sheets and tubules throughout
185 the cell cytoplasm, some of which were juxtaposed to dextran-labelled lysosomes **(Fig. 2A, Sup.**
186 **Fig. S1A).** Strikingly, the ER network was visibly distorted, exhibiting numerous "black holes" in
187 cells treated with apilimod **(Fig. 2A)** and YM-201636 **(Sup. Fig. S1A).** Many of these voids, but
188 not all, were occupied with Alexa647-dextran **(Fig. 2A, Sup. Fig. S1A).** To determine if some of
189 these voids were cytosolic in nature or contoured by other swollen early endosomal structures,
190 we expressed cytosolic mCherry or mCherry-Rab5. None of the apparent ER-decorated voids
191 labelled with cytosolic mCherry (**Sup. Fig. 2A**), but a subpopulation was lined with mCherry-
192 Rab5 **(Sup. Fig. S2B).** Overall, the ER "black holes" were occupied with either dextran-labelled
193 lysosomes or mCherry-Rab5 endosomes **(Sup. Fig. S2C-D)**, indicating that separate populations
194 of enlarged endosomal and lysosomal organelles may alter the ER architecture. To complement
195 our visual inspection and buttress these assertions, we quantified the ER morphology by

196 extracting total ER skeletal length, number of branches and junctions per cell, and average
197 branch length (depicted in **Fig. 2B, 2C**). Apilimod and YM201636 both caused a significant
198 decline in ER total skeletal length, loss of ER junctions and branch numbers, though not for ER
199 branch length **(Fig. 2D-G** and **Sup. Fig. S1B-E).** Importantly, these changes were not due to an
200 acute and transient effect of PIKfyve inhibition since cells silenced for *VAC14* for 48 h displayed
201 the expected enlarged lysosomes and distorted ER morphometrics (**Sup. Fig. S3**). Collectively,
202 these data show a reduction in total ER network size and loss of the ER interconnectivity in cells
203 negated for PIKfyve activity.
204
205 *Loss of PIKfyve activity impairs ER dynamics*
206 We next examined whether ER motility was disturbed in PIKfyve-inhibited cells. To assess this,
207 we employed a previously described method that measures membrane displacement by
208 tracking pixel intensity changes over time (Spits et al., 2021). To achieve this, we tracked ER-
209 mNeonGreen pixels over time in control and PIKfyve-hindered cells, binning pixel displacement
210 into three categories: low (displacement of 0-3 pixels), intermediate (displacement of 4-7
211 pixels), and rapid ER movement (8 or more pixels; **Fig. 3A**). Relative to vehicle-treated cells, cells
212 exposed to apilimod or YM201636 displayed a greater number of pixels with low membrane
213 displacement and a corresponding drop in pixels with rapid membrane displacement **(Fig. 3B-E**;
214 **Sup. Fig. S1F-I**; **Sup. Videos 1-3**). These results reveal that the ER is less motile in cells arrested
215 for PIKfyve activity, further reinforcing the idea that lysosomal coalescence distorts ER
216 architecture and dynamics.
217

218 *ER hitchhiking is blunted in PIKfyve-perturbed cells*

219 Conceivably, the distortion of the ER spatio-temporal properties in PIKfyve-deficient cells could
220 simply arise from physical hindrance of swollen endo-lysosomes compressing the intricate ER
221 network of tubules and sheets. While physical hindrance of swollen lysosomes may very well
222 help disfigure the ER network, we noted that there were few swollen lysosomes in the
223 periphery of PIKfyve-inhibited cells (quantified below), which nevertheless sustained loss of ER
224 complexity. We thus postulated that a more sophisticated mechanism was at play.

225 The ER is partly sculpted by forming and extending new ER tubules, which can then fuse
226 with existing tubules to promote ER interconnectivity (Westrate et al., 2015; Guo et al., 2018;
227 Shibata et al., 2010; Spits et al., 2021). There are several processes that drive ER shaping that
228 depend on microtubules: ER sliding, TAC-dependent ER extension, and ER hitchhiking (Spits et
229 al., 2021; Grigoriev et al., 2008; Rodríguez-García et al., 2020; Guo et al., 2018; Shibata et al.,
230 2010). We thus investigated whether perturbation of some of these processes contributed to
231 changes in ER spatial-temporal dynamics in PIKfyve-negated cells.

232 First, using immunofluorescence against α-tubulin to analyze microtubule morphology,
233 we did not perceive a significant difference in microtubule organization between vehicle and
234 apilimod-treated cells **(Sup. Fig. S4A)** when quantifying parameters such as number of
235 microtubule branches and junctions per cell, and average microtubule branch length **(Sup. Fig.**
236 **S4B-D)** – this despite visibly enlarged lysosomes in apilimod-treated cells**.** This was also true
237 for the number and kinetics of EB1-GFP comets, which associate with microtubule plus-ends
238 **(Sup. Fig. S4E-H; Sup. Videos 4-6).** We then measured ER hitchhiking events by tracking ER and
239 lysosome movement over one-minute movies at 0.3 Hz. Timelapses were then analysed for

240 lysosome-ER co-migration in control and PIKfyve-inhibited cells. We observed an average of 4-6
241 hitchhiking events/min/100 μm^2 area in control cells, which substantially dropped to 0-1
242 events/min/100 μm^2 in apilimod-exposed cells **(Fig. 3F, G; Sup. Videos 7-8).** These observations
243 support a model whereby the botched ER morphology and dynamics in PIKfyve-defective cells
244 are partly underpinned by failed ER hitchhiking.
245
246 *Lysosome distribution and movement are altered in PIKfyve-inhibited cells*
247 Hitchhiking requires the ER to attach to a endosome/lysosome and for the endosome/lysosome
248 to move (Spits et al., 2021; Pedersen et al., 2020; Voeltz et al., 2024). We thus reasoned that
249 abrogation of ER hitchhiking in PIKfyve-hindered cells may ensue from a defect in attachment
250 and/or lysosome motility. We first tested lysosome motility and distribution in control and
251 PIKfyve-impaired cells. Using shell analysis, we reveal that lysosomes collapse into the
252 perinuclear region and become less frequent in the cell periphery in the absence of PIKfyve
253 activity **(Fig. 4A-C).** This was accompanied by a significant decline in lysosome speed and total
254 distance travelled in apilimod-treated COS-7 cells relative to vehicle-treated cells (**Fig. 4D-F),**
255 made visible through kymographs that revealed a marked decrease in the motility of lysosomes
256 upon PIKfyve inhibition (**Fig. 4G)**. Collectively, loss of PIKfyve activity is associated with hindered
257 lysosome motility and displacement to the perinuclear region. This implies that in the absence
258 of PIKfyve activity, lysosomes likely sustain a loss of kinesin and/or hyperactivation of dynein
259 activities. As a corollary, this could impair ER hitchhiking and disrupt the ER network.
260
261 *PIKfyve inhibition alters ER-lysosome contact sites*

262 There are likely several types of ER-lysosome contact sites (Rudnik et al., 2024; Raiborg et al.,
263 2015a; Allison et al., 2017; Du et al., 2023; Bonet-Ponce and Cookson, 2022; Cai et al., 2022;
264 Gao et al., 2022; Saric et al., 2021). Nonetheless, contact sites formed by the ER
265 transmembrane proteins, protrudin and VAPA/B, and the lysosomal Rab7 GTPase, are linked to
266 lysosome and ER position and motility via kinesin (Pedersen et al., 2020; Raiborg et al., 2015a;
267 Matsuzaki et al., 2011). Therefore, we tested if PIKfyve blockade altered the protrudin-VAPA-
268 Rab7 contact site by using proximity ligation assays (PLAs) – representative figures of negative
269 controls for each PLA pair are shown in **Sup. Fig. S5A-H**.

270 We found that protrudin and VAPA appeared proximal in equal measures between
271 PIKfyve-enabled and PIKfyve-blocked cells **(Fig. 5A, D)**, which is perhaps not surprising since
272 both are ER transmembrane proteins. However, we observed an inverse relationship between
273 Rab7 and these proteins: there were fewer proximal events between VAPA and Rab7 (**Fig. 5B,**
274 **E)**, but higher between protrudin and Rab7 **(Fig. 5C, F)**. Perhaps consistent with this, we did not
275 observe a change in total Rab7 associated with LAMP1 by immunofluorescence in these cells
276 and experimental conditions (**Sup Fig. S5I-K)**. Similarly, we did not observe a change in the
277 cellular levels of GTP-loaded Rab7 as reported by affinity precipitation of GTP-bound Rab7 using
278 GST-RILP-C33 in HeLa cells **(Sup Fig. S5L-M)**, though it is possible that specific pools of GTP-Rab7
279 may be altered in these conditions. This suggests that PIKfyve inactivation does not lead to a
280 wholesale loss or enhancement of this membrane contact type but instead may be altering its
281 conformation.

282 Protrudin-Rab7-VapA are proposed to load kinesin onto the Rab7-FYCO1 complex
283 (Matsuzaki et al., 2011; Raiborg et al., 2015a; b; Pankiv et al., 2010). Moreover, PIKfyve and

284 PtdIns(3,5)P_2 may regulate kinesin-5 on precursor vesicles in neurons (Rizalar et al., 2023).
285 Given our observations above and the collapse of lysosome motility and perinuclear
286 accumulation, we next determined if PIKfyve inactivation altered the relative proximity of
287 FYCO1 and kinesin-1 with these proteins. Unfortunately, we could not test the proximity
288 between protrudin and kinesin-1 due to the lack of compatible antibodies. Collectively, there
289 was an increase in proximity events between FYCO1 and Rab7 and VAPA, but no change in
290 proximity events with protrudin (**Fig. 5G-I, 5L-N**). Importantly, there was a significant drop in
291 FYCO1 and kinesin-1 proximity (**Fig. 5J, 5O**), which did not translate to altered Rab7 and kinesin-
292 1 proximity (**FIG. 5K, 5P)**.

293 Overall, these data suggest that PIKfyve suppression reorganizes the conformation of
294 the Rab7-VAPA-protrudin ER-lysosome contact site, whereby protrudin-Rab7 interaction is
295 promoted at the expense of Rab7-VAPA proximity**.** Similarly, FYCO1 may be overly recruited to
296 Rab7 and proximal to VAPA at the expense of kinesin-1 interaction, which may lead to reduced
297 lysosome anterograde movement. Since PIKfyve inhibition concomitantly increases PtdIns(3)P
298 while reducing PtdIns(3,5)P_2 levels (Choy et al., 2018; Zolov et al., 2012) and protrudin and
299 FYCO1 have a FYVE domain, we postulate that the excess PtdIns(3)P causes hyper-tethering
300 onto lysosomal membranes. In fact, since protrudin is an ER transmembrane protein, we
301 propose that hyper-stabilization of protrudin-Rab7 interaction via excess PtdIns(3)P alters the
302 ER morphology.

303

304 *Protrudin and PtdIns(3)P are required for ER distortion upon PIKfyve inhibition*

305 To test the hypothesis that protrudin drives ER distortion in the absence of PIKfyve activity, we
306 quantified ER morphometrics in cells expressing ER-mScarletI, silenced for protrudin, and
307 treated with apilimod. Surprisingly, protrudin silencing had no discernible effects on ER
308 morphometrics in vehicle-treated cells (**Sup. Fig. S6A, B**; **Fig. 6A, 6C-D**), implying that protrudin
309 does not have an essential role in defining basal ER morphology, or that redundant factors are
310 at play. Similarly, protrudin silencing did not disturb lysosome volume or size (**Fig. 6B, 6E-F**). By
311 contrast, protrudin silencing partially, but substantially offset the effects of apilimod on ER
312 morphology (**Fig. 6A, 6C-D**), but not on lysosome metrics (**Fig. 6B, 6E-F**), indicating that
313 protrudin is required for ER distortion in the absence of PIKfyve activity. We then treated ER-
314 mNeonGreen-expressing cells with VPS34-In1, an inhibitor of VPS34, to block PtdIns(3)P and to
315 determine if this lipid was also required for ER morphological changes during PIKfyve
316 inactivation (**Fig. 6G**). Unlike apilimod alone, which changed ER morphometrics (**Fig. 6H, I**) and
317 lysosome properties (**Fig. 6J, K**) relative to vehicle, VPS34-In1 alone and VPS34-In1 together
318 with apilimod were not statistically different from vehicle for ER morphometrics (**Fig. 6H, I**) and
319 lysosome properties (**Fig. 6J, K;** though lysosomes appeared somewhat enlarged). Together,
320 these data intimate a role for protrudin and PtdIns(3)P in the reorganization of ER morphology
321 triggered by PIKfyve inactivation.
322
323 *Protrudin lipid tethering mechanisms are altered upon PIKfyve inhibition*
324 We next expressed GFP-chimeras of wild-type (protrudin^{wt}) and a FYVE4A-mutant protrudin
325 (protrudin^{FYVE4A}; (Raiborg et al., 2015a)) in cells expressing and/or silenced for endogenous
326 protrudin (**Fig. 7A**). Protrudin^{wt}-GFP and protrudin^{FYVE4A}-GFP both exhibited ER-like distribution

327 in the presence of (non-targeting) or the absence of endogenous protrudin (siRNA; **Fig. 7A**).
328 Remarkably, cells expressing protrudin^{wt}-GFP but inhibited for PIKfyve displayed intense
329 protrudin^{wt}-GFP ring structures that decorated both dextran-labelled and dextran-negative
330 vacuoles (**Fig. 7A**). Since protrudin is an ER-transmembrane protein, this means that the ER
331 membrane or regions of the ER membrane wrap around vacuoles induced in PIKfyve-disabled
332 cells. This concept is supported by 3D reconstruction of protrudin^{wt}-GFP, which extends and at
333 least partially encloses dextran-loaded vacuoles (**Sup. Fig. S6C**). Importantly, the
334 protrudin^{FYVE4A}-GFP mutant failed to form these rings around dextran-loaded lysosomes in
335 PIKfyve-inhibited cells (**Fig. 7A**), indicating that the protrudin-labelled ER membranes tightly
336 encircle the enlarged lysosomes, likely in a PtdIns(3)P-dependent manner. Consistent with this,
337 apilimod-treated cells displayed intense 2FYVE-RFP vacuoles that were reduced upon VPS34-In1
338 exposure, suggesting high PtdIns(3)P levels (**Fig. 7D**).

339 We then determined if excess protrudin wrapping around vacuoles was at least partially
340 responsible for the altered ER morphometrics in PIKfyve-arrested cells by skeletonizing the
341 protrudin-GFP fluorescence. First, protrudin-GFP-based ER morphometrics was
342 indistinguishable when cells were mock-silenced or silenced for endogenous protrudin (**Fig. 7B-**
343 **C**, first two columns). Second, apilimod elicited dramatic changes to ER morphometrics in cells
344 expressing wild-type protrudin-GFP, whether mock or silenced for endogenous protrudin (**Fig.**
345 **7B-C**, compare columns 1 and 3, and 2 and 4). We then compared the ER morphometrics by
346 expressing protrudin^{FYVE4A}-GFP in cells silenced for endogenous protrudin. In vehicle-treated
347 cells, the ER morphology was like those expressing protrudin^{wt}-GFP (**Fig. 7B-C**, compare
348 columns 2 and 5). Yet, the ER changes driven by apilimod were annulled in cells expressing

349 protrudin^{FYVE4A}-GFP relative to protrudin^{wt}-GFP (**Fig. 7B-C**, compare columns 4 and 6).
350 Additionally, protrudin^{wt}-GFP vacuoles were mostly eliminated when VPS34-In1 was co-
351 incubated with apilimod (**Fig. 7E**), which partially recovered the ER morphology based on
352 protrudin^{wt}-GFP fluorescence (**Fig. 7F, G**), despite altered lysosome morphometrics (**Fig. 7H, I)**.
353 Thus, a functional FYVE domain on protrudin and PtdIns(3)P are necessary for the apilimod-
354 induced changes to ER morphometrics.

355 Since protrudin interacts with sculpting factors as well, we also assessed the distribution
356 of Atlastin-1, CLIMP63, and Rnt4a. First, and as expected, apilimod changed the ER
357 morphometrics based on overexpressed CLIMP63, Rtn4, and Atlastin (**Sup. Fig. S7A-F, H-I**).
358 Secondly, apilimod-treated cells formed rings of Atlastin-1 (**Sup. Fig. S7G**) that were less
359 prominent than protrudin-GFP (**Fig. 7**); CLIMP63 and Rtn4a rings were even less prominent, but
360 visible (**Fig. 1A, B**). Together, it may be that the nanoscale organization of ER sculpting factors
361 could further contribute to ER remodeling in PIKfyve-impaired cells.

362

363 *Excess protrudin lipid tethering during PIKfyve inhibition alters ER-lysosome contacts*

364 We then explored if the absence of PtdIns(3)P or expression of protrudin^{FYVE4A}-GFP rescued the
365 relative proximity of protrudin-Rab7 and Rab7-VAPA in PIKfyve-defective cells. First, as a
366 control, we note that protrudin silencing eliminated the number of proximity events between
367 Rab7-protrudin PLA (**Fig. 8A, C)** and Rab7-VAPA PLA **(Fig. 8B, D),** the latter result suggesting
368 protrudin cannot be removed without disturbing the contact sites containing Rab7 and VAPA.
369 Third, we compared the proximity of these proteins in cells expressing protrudin^{wt}-GFP or
370 protrudin^{FYVE4A}-GFP upon endogenous protrudin silencing **(Fig. 8E)**. As before, apilimod

371 promoted Rab7-protrudin interactions in cells expressing endogenous (Fig. 8E, columns 1 and 4)
372 and protrudin^{wt}-GFP (**Fig. 8E,** columns 2 and 5). Importantly, there was no difference between
373 vehicle and apilimod-treated cells expressing protrudin^{FYVE4A}-GFP (**Fig. 8E,** columns 3 and 6) and
374 a significant distinction between protrudin^{wt}-GFP and protrudin^{FYVE4A}-GFP with apilimod (**Fig. 8E**,
375 columns 5 and 6).

376 Overall, we propose that PIKfyve inhibition leads to excess PtdIns(3)P levels, which
377 inappropriately recruits and locks protrudin to lysosomes via its FYVE domain. This hyper-
378 recruitment distorts the balance of ER-lysosome contact sites by shifting interactions toward
379 Rab7-protrudin tethering and away from a conformation wherein Rab7-VapA are more
380 proximal. The disproportionate lysosomal localization of protrudin also disrupts ER morphology.
381

382 *Enforced ER-lysosome contacts suffice to disrupt ER morphology*

383 Our data suggest that PIKfyve inhibition accumulates PtdIns(3)P that hyper-tethers protrudin on
384 lysosomes, disrupting the ER morphology. To test whether hyper-tethering of protrudin to
385 lysosomes sufficed to disturb the ER architecture, we employed the FKBP-FRB inducible
386 dimerization system by expressing iRFP-FRB-Rab7 and newly engineered FKBP-mCherry-
387 protrudin^{WT} or FKBP-mCherry-protrudin^{FYVE4A} constructs. Without rapamycin, and based on
388 their fluorescent signal, the ER morphometrics appeared normal for both WT and protruin^{FYVE4A}
389 and no obvious wrapping of ER occurred around Rab7 puncta (**Fig. 9A).** In remarkable contrast
390 to this, addition of rapamycin to dimerize the FKBP and FRB chimeric proteins, caused extreme
391 ER wrapping around Rab7-positive lysosomes that strongly distorted ER morphometrics both
392 for protrudin^{WT} and protrudin^{FYVE4A} (**Fig. 9A, 9B-D**, compare columns 1 and 2 with 3 and 4,

393 respectively). Additionally, VPS34-In1, which could reverse changes to ER morphometrics by
394 apilimod and GFP-protrudin (**Fig. 7E-G**), was impotent at rescuing the rapamycin-induced ER
395 morphological changes and wrapping around lysosomes (**Fig. 9**). Overall, these data
396 demonstrate that enforced ER-lysosome contact suffices to disturb ER morphology and bypass
397 the need for the protrudin's FYVE domain and PtdIns(3)P. In conclusion, this supports that the
398 ER morphological changes we observed during PIKfyve inactivation are driven by excess
399 PtdIns(3)P and hyper-tethering of protrudin to lysosomes.
400

401 **Discussion**

402 PIKfyve is a well-established regulator of the endolysosomal pathway (Choy et al., 2018; Bissig
403 et al., 2017; Sbrissa et al., 2002; Ikonomov et al., 2001; Sharma et al., 2019). Here, we extend
404 PIKfyve's sphere of influence by revealing that PIKfyve activity affects ER morphology and
405 dynamics – cells inhibited for PIKfyve activity present a less reticulate and dynamic ER,
406 ostensibly driven in part by two mechanisms. First, the enlarged lysosomes become less motile,
407 collapsing to the cell centre – as a corollary, we observed fewer ER hitchhiking events, which
408 promotes ER remodelling and motility (Spits et al., 2021; Guimaraes et al., 2015; Langley et al.,
409 2025; Lu et al., 2020). Second, the ER membrane appears "glued" to enlarged lysosomes by
410 extensive protrudin-dependent binding, likely due to a surfeit of PtdIns(3)P (Choy et al., 2018;
411 Zolov et al., 2012). Thus, we identified an important role for PIKfyve in modulating ER
412 properties beyond those known for the endo-lysosomal system.
413

414 *PIKfyve modulation of lysosome and ER architecture*

415 Inhibition of PIKfyve and PtdIns(3,5)P_2 elicits lysosome coalescence (Choy et al., 2018; Bissig et
416 al., 2017; Sharma et al., 2019). Currently, we do not know if this occurs due to dysregulation of
417 fission factors in mammalian cells like the recently discovered HPO-27 (Li et al., 2024), and/or
418 through regulation of ion signaling modulated by channels like TPCs, TRPLM1, and ClC7 (Leray
419 et al., 2022; Dong et al., 2010; Wang et al., 2012), or through a different mechanism. Given that
420 ER tubules contact and demarcate sites of mitochondrion and endosome fission (Rowland et al.,
421 2014; Friedman et al., 2013, 2011), we sought to test if PIKfyve and ER-dependent fission were
422 linked by overexpressing CLIMP63 and Rtn4a to respectively abate and promote ER tubule
423 formation. We reasoned that promoting sheets, CLIMP63 overexpression would lead to
424 enlarged lysosomes, mimicking PIKfyve arrest, while excess Rtn4a might rescue lysosome
425 coalescence in PIKfyve-hindered cells by promoting ER tubules; however, we did not discern
426 these predicted behaviours. While we observed effects on individual lysosome volume in
427 CLIMP63/Rnt4a-modified cells, this was not accompanied by altered lysosome number,
428 suggesting that the effects on lysosome size are not because of altered fusion-fission cycling, as
429 is the case for PIKfyve (Choy et al., 2018; Sharma et al., 2019). Instead, we anticipate that
430 processes such as modified biosynthesis and/or lipid transfer may drive these changes in
431 lysosome size. It remains possible that CLIMP63 and Rtn4a overexpression are not ideal
432 approaches to test the relationship between PIKfyve-driven processes and ER.

433 Conversely, disturbing PIKfyve greatly perturbed the ER architecture, which became less
434 reticulated and more sheet-like, decorated with various spherical “voids” filled with enlarged
435 lysosomes or endosomes. While some of these ER morphometric changes may reflect steric
436 hindrance by the enlarged endosomes and lysosomes, our data point to a more elegant role for

437 PIKfyve in modulating ER properties – by calibrating PtdIns(3)P levels to balance protrudin-
438 dependent ER-lysosome contact sites. Supporting this model, ER morphometrics were partly
439 rescued in PIKfyve-inhibited cells by *i)* VPS34-In1 co-administration with apilimod, *ii)* silencing of
440 endogenous protrudin, and *iii)* re-expression of the FYVE4A-protrudin mutant, but not of the
441 wild-type protrudin – all despite enlarged lysosomes. Convincingly, artificially clamping ER to
442 lysosomes with rapamycin-inducible system sufficed to alter ER morphometrics even in the
443 absence of PtdIns(3)P (**Fig. 9**). Thus, we propose that physical "glueing" of the ER membrane to
444 lysosomes likely helps transform the ER architecture in PIKfyve-defective cells. However,
445 physical obstruction by enlarged endosomes and lysosomes and nanoscale re-organization of
446 ER morphogenic factors like CLIMP63, Atlastin-1, and reticulons may also contribute to ER
447 remodeling in the absence of PIKfyve activity since these proteins interact with protrudin
448 (Chang et al., 2013; Hashimoto et al., 2014).
449
450 *PIKfyve modulates lysosome and ER dynamics*
451 A striking consequence of PIKfyve inhibition is the concurrent loss of lysosome and ER motility,
452 which we propose are related processes. While microtubule morphometrics and dynamics
453 appeared nearly normal in PIKfyve-inhibited cells, the enlarged lysosomes were perinuclear and
454 less motile. While we do not know how PIKfyve modulates lysosome dynamics, an attractive
455 mechanism is that PIKfyve tightly balances PtdIns(3)P and PtdIns(3,5)P_2 levels in space and time
456 to govern various PtdIns(3)P-interacting proteins such as FYCO1, RUFY3, RUFY4, protrudin, and
457 SNX19, most of which modulate motor function (Pankiv et al., 2010; Saric et al., 2021; Raiborg
458 et al., 2015a; Jongsma et al., 2024; Kumar et al., 2022; Keren-Kaplan et al., 2022; Jongsma et al.,

459 2016, 2024). Remarkably, our observations on protrudin behaviour align well with previous
460 work by Saric *et al. on* SNX19, another ER transmembrane protein that carries a PX domain that
461 binds to PtdIns(3)P (Mas et al., 2014; Saric et al., 2021). These authors observed that SNX19
462 forms an ER-lysosome contact site that restricts endo-lysosome motility and that enlarged
463 lysosomes in PIKfyve inhibited cells were extensively decorated with SNX19 and were less
464 motile (Saric et al., 2021). Collectively, it is intriguing to consider that PIKfyve is not just
465 important to synthesize PtdIns(3,5)P_2, but crucial to tightly modulate the levels and location of
466 PtdIns(3)P to coordinate these proteins. Temptingly, this may explain the existence of the
467 conserved PIKfyve complex, which holds together the PIKfyve and the antagonistic Fig4 lipid
468 phosphatase (Botelho et al., 2008; Jin et al., 2008; Sbrissa et al., 2007; Botelho, 2009) – to
469 exquisitely switch between PtdIns(3)P and PtdIns(3,5)P_2 at spatially-restricted sites like
470 membrane contacts. This phosphoinositide-based switch may interface with the previously
471 observed role of repeated ER-endosome contacts and microtubule-associated proteins in
472 swapping motor activity on endosomes (Raiborg et al., 2015a; Jongsma et al., 2024), and
473 regulation of ions like Ca^{2+}(Li et al., 2016)a.

474 As for loss of ER dynamism, we propose that this is partly due to declined lysosome
475 motility, and consequently, reduced ER hitchhiking, which is a major driver of ER remodeling
476 (Spits et al., 2021; Lu et al., 2020). However, ER hitchhiking also depends on the formation of
477 lysosome-ER contact sites. Based on our observations, ER-lysosome contact sites not only form,
478 but may in fact undergo hyper-tethering during PIKfyve arrest as visualized for protrudin by us
479 and for SNX19 by *Saric et al*, both of which indicate that ER membrane subdomains envelope
480 enlarged lysosomes and related organelles. This implies that bidirectional transport of

481 lysosomes and ER may depend on regulated conformational or compositional changes to these
482 contacts, which consequently alter kinesin and/or dynein-mediated activity, discussed next.
483
484 *PIKfyve and regulation of ER-lysosome contact sites*
485 Protrudin is thought to load kinesin-1 onto FYCO1 on lysosomes (Raiborg et al., 2015a). To do
486 this, protrudin binds to PtdIns(3)P and Rab7 on lysosomes and VAPA on the ER membrane
487 (Raiborg et al., 2015a). Nonetheless, there is little known about the structural organization of
488 these proteins at these contact sites – for example, we do not know if all interactions are
489 concurrent, sequential, or if subject to conformational changes. Since PIKfyve inhibition did not
490 lead to a wholesale loss or gain in proximity events between protrudin, VAPA, Rab7, FYCO1, and
491 kinesin-1, this suggests that PIKfyve activity aids in a conformational or selective compositional
492 change at these sites. For example, protrudin-Rab7 and Rab7-FYCO1 proximity increased, while
493 VAPA-Rab7 and FYCO1-kinesin1 decreased in PIKfyve-inactive cells. Importantly, apilimod-
494 enhanced Rab7-protrudin proximity events depended on a functioning FYVE domain of
495 protrudin. Collectively, we propose a model whereby PIKfyve converts PtdIns(3)P to
496 PtdIns(3,5)P_2 to transiently promote protrudin dissociation from lysosomal membranes and
497 elicit a conformational change that helps modulate kinesin-1 loading and/or activity. Of course,
498 PtdIns(3,5)P_2 itself may have a regulatory role in this process, but we do not know the targets of
499 this lipid in this context, if any.
500
501 *Conclusion*

502 Collectively, our results suggest that PIKfyve supports ER network integrity by governing
503 lysosome dynamics, distribution, and ER-lysosome contact sites. In the absence of PIKfyve,
504 swollen and immobile lysosomes gain excess PtdIns(3)P that hyper-tether ER-lysosomes via
505 protrudin, trapping these in a non-productive conformation that alters ER architecture and
506 hitchhiking. These results illuminate a previously underappreciated aspect of PIKfyve function
507 and provide mechanistic insight into how lysosomal dysfunction can drive architectural and
508 dynamic changes of neighbouring organelles. Moreover, the PIKfyve pathway is linked to
509 neurological diseases and is a potential therapeutic target against certain cancers and viral
510 infections (Chow et al., 2007; Cai et al., 2013; Babu et al., 2024; Cheng et al., 2025; Bao et al.,
511 2023; Kang et al., 2020). The physiological link between the PIKfyve pathway and these diseases
512 is generally thought to occur through changes to the endo-lysosomal pathway. However, given
513 our findings, mutations in the PIKfyve pathway that lead to disease may reflect altered ER
514 function as well, particularly in highly secretory or polarized cells where proper ER architecture
515 and dynamics are critical.
516
517
---
518 **Methods and Materials**
519 *Cell culture*
520 COS-7 and HeLa cell strains were cultured in Dulbecco's Modified Eagle Medium (DMEM;
521 Wisent, St. Bruno, QC) and U2OS-wt cells were cultured in 50% Dulbecco's Modified Eagle
522 Medium / 50% F-12 with L-glutamine and HEPES buffer (F-12/DMEM; Gibco, New York, USA)
523 supplemented with 10% heat-inactivated fetal bovine serum (FBS; Wisent) and 1% penicillin-

524 streptomycin (10,000 U/mL) (P/S; Gibco, Burlington, ON). All cells were authenticated, checked
525 for contamination and cultured at 37°C with 5% CO_2.
526
527 *Plasmids, siRNA gene silencing, and transfection*
528 Plasmids obtained from Addgene were as follows: ER-mNeonGreen (#137804) and ER-mScarletI
529 (#137805) were described in (Chertkova et al., 2020); pHAGE2 GFP-Rtn4a (#86684) and pHAGE2
530 GFP-Atlastin1 (#86678) were described in (Wang et al., 2016); mCherry-CLIMP63 (#136293,
531 (Shibata et al., 2008)); eGFP-KIF5B (#172203, (Guardia et al., 2016)); pmRFP-C3::Rab5 (#14437,
532 (Vonderheit and Helenius, 2005)); iRFP-FRB-Rab7 (#51613; (Hammond et al., 2014)); pcDNA3.1-
533 mCherry (#128744), pcDNA3-eGFP (#13031), and pEGFP-N1::human EB1 (#39299). The plasmid
534 encoding 2xFYVE-RFP was a gift from Dr. Amra Saric at the Hospital for Sick Children. We note
535 that ER-mNeonGreen and ER-mScarletI are fusions of the mNeonGreen and mScarletI
536 fluorescent proteins to the KDEL ER-retention signal, respectively (Chertkova et al., 2020).
537 Plasmids encoding protrudin^{WT}-GFP, protrudin^{FYVE4A}-GFP were a kind gift from Dr. Camilla
538 Raiborg (Oslo University Hospital) and was previously described (Raiborg et al., 2015a).
539 Plasmids encoding protrudin^{WT} or protrudin^{FYVE4A} mutant fused to FKBP-mCherry were
540 generated by GenScript (Piscataway, NJ, USA). Protrudin sequences were cloned at the C-
541 terminus of the FKBP-mCherry construct. The FKBP-mCherry backbone (Addgene plasmid
542 #108122) was originally generated by Gerry Hammond. Protrudin DNA sequences were kindly
543 provided by Eva Maria Wenzel (Institute for Cancer Research, Oslo, Norway). Transient
544 transfections were performed with FuGENE HD (Promega, Madison, WI) following the

545 manufacturer's instructions, using a 3:1 DNA to transfection reagent ratio. The transfection
546 mixture was replaced with fresh medium after 4-6 h and cells were used 24 h post-transfection.
547 Silencing RNA oligonucleotides were transfected into HeLa and U2OS cells with
548 Lipofectamine RNAiMAX Transfection Reagent (Invitrogen, Carlsbad, CA) following the
549 manufacturer's instructions. For protrudin silencing, one round of knockdown was performed
550 using 25 nM ON-TARGETplus ZFYVE27 (the standard gene name for protrudin) individual siRNA
551 (Horizon Discovery, Dharmacon; J-016349-12-0010) or ON-TARGETplus non-targeting control
552 (Horizon Discovery, Dharmacon) over 24 h. For Vac14 silencing, one round of knockdown was
553 performed using 25 nM ON-TARGETplus Vac14 siRNA individual siRNA 1 (Horizon Discovery,
554 Dharmacon; Oligo 8, J-015729-08-005) and siRNA 2 (Horizon Discovery, Dharmacon; Oligo 5, J-
555 015729-05-005) or ON-TARGETplus non-targeting control (Horizon Discovery, Dharmacon) over
556 48 h.
557
558 *Organelle labelling*
559 Lysosomes in COS-7 were labelled with 320 µg/mL Alexa-Fluor 488-, 546- or 647-conjugated
560 dextran (ThermoFisher), while lysosomes in HeLa and U2OS-wt cells were labelled with 150
561 µg/mL of fluorescent dextran by incubating cells in cell-specific complete medium for 1 h at
562 37°C with 5% CO_2, followed by washing in phosphate-buffered saline (PBS) and replenishing
563 with fresh complete medium for 1 h before live-cell imaging (Choy et al., 2018; Ohkuma and
564 Poole, 1978; Ferris et al., 1987). Since this method likely labels a spectrum of late endosomes,
565 lysosomes and endolysosomes, the term *lysosomes* reflects this range of organelles in this
566 work. mCherry-Rab5 labels early endosomes, specifically (Vonderheit and Helenius, 2005; Bucci

567 et al., 1992; Chavrier et al., 1990). ER-mNeonGreen and ER-ScarletI were used to label bulk ER
568 (Chertkova et al., 2020).
569
570 *Pharmacological treatments*
571 PIKfyve inhibition was accomplished by treating cells with 80-240 nM apilimod (Selleck
572 Chemicals LLC, Houston, TX) or 1 µM YM-201636 (Cayman Chemical Company, Ann Arbor, MI)
573 for 1-2 h – specific concentrations and times are indicated in each figure legend. Vps34 Class III
574 PI 3-kinase was arrested by treating cells with 1 µM VPS34-In1 (Chemical Company, Ann Arbor,
575 MI) for 2 h, and when used in combination with apilimod, VPS34-In1 was co-incubated for 2 h.
576
577 *Immunofluorescence*
578 For immunofluorescence, following treatments, cells were fixed with 4% paraformaldehyde
579 (PFA; v/v) for 15 min. After washing with PBS, residual PFA was quenched with 100 mM glycine
580 for 10 min, then cells were blocked and permeabilized with 0.1% (v/v) Triton X-100 for 5 min.
581 Cells were then subjected to mouse monoclonal (DM1A) antibody against α-tubulin (1:100;
582 #T9026; Sigma-Aldrich), rabbit monoclonal (D9F52) antibody against Rab7 (1:100; #9367),
583 mouse monoclonal (E9O7E) antibody against Rab7 (1:100; #95746), mouse monoclonal (D4O1S)
584 antibody against LAMP1 (1:100; #15665) and rabbit monoclonal (D2D11) antibody against
585 LAMP1 (1:200; #9091; all from Cell Signaling Technology). Dylight-conjugated secondary donkey
586 antibodies against rabbit and mouse (1:1000; Novus Biologicals Canada) were used.
587
588 *Proximity ligation assays*

589 PLA was performed with Duolink In Situ Red Starter Kit Mouse/Rabbit (Sigma Aldrich,
590 DUO92101) according to the manufacturer's instructions. Briefly, HeLa cells were seeded, fixed
591 with 4% PFA for 15 min, quenched with 100 mM glycine for 10 min and permeabilized with
592 0.1% Triton X-100 for 5 min – all at RT respectively. Cells were co-incubated with one mouse
593 and one rabbit antibody from the following; rabbit monoclonal (D9F52) antibody against Rab7
594 (1:100; #9367; Cell Signaling Technology), mouse monoclonal (E9O7E) antibody against Rab7
595 (1:100; #95746; Cell Signaling Technology), mouse monoclonal (4C12) antibody against VAPA
596 (1:100; #293278; Santa Cruz Biotechnology), rabbit polyclonal antibody against ZFYVE27 (1:100;
597 12680-1-AP; Proteintech), rabbit monoclonal (E3H4J) antibody against KIF5B (1:250; #47610;
598 Cell Signaling Technology), rabbit polyclonal antibody against FYCO1 (1:250; 25730-1-AP;
599 Proteintech), rabbit and mouse monoclonal (5G4) antibody against GFP (1:500; #55494; Cell
600 Signaling Technology), followed by incubation with PLA probes. After probe incubation, cells
601 were washed and incubated with ligation mixtures to promote DNA ligation. Next, amplification
602 mixtures were added to cells for Rolling Circle Amplification (RCA) and hybridization of
603 fluorescently labelled oligonucleotides to occur. A PLA mounting media containing DAPI was
604 added to washed cells when mounted. PLA signals from cells were detected using confocal
605 microscopy.
606
607 *Fluorescence microscopy*
608 Confocal images were obtained using a Quorum Diskovery spinning disc confocal system
609 (Quorum Technologies, Inc., Guelph, ON), a Quorum ReSCAN confocal system (Quorum
610 Technologies, In., Guelph, ON) and a Olympus CSU spinning disc confocal system (Evident

611 Scientific, Tokyo, Japan). The Diskovery microscope consisted of an inverted fluorescence
612 microscope (DMi8; Leica) equipped with an Andor Zyla 4.2 Megapixel sCMOS camera (Oxford
613 Instruments, Belfast, UK), a 63x oil immersion objective (1.4 NA), and standard excitation and
614 emission filter sets and lasers were used for all fluorophores. The microscope system was
615 controlled by the MetaMorph acquisition software (Molecular Devices, LLC, San Jose, CA, USA).
616 The ReSCAN microscope consisted of an inverted fluorescence microscope (DMi8 Automated;
617 Leica) equipped with a ORCA-Flash V3 digital sCMOS camera (Hamamatsu, Shizuoka Prefecture,
618 Japan) , a 63x oil immersion objective (0.6 to 1.4 NA) , and standard excitation and emission
619 filter sets and lasers were used for all fluorophores. The microscope system was controlled by
620 the Volocity acquisition software (Quorum Technologies, In., Guelph, ON). The Olympus
621 spinning disc microscope consisted of an inverted fluorescence microscope (IX83, Olympus)
622 equipped with a ORCA-Flash4.0 V3 sCMOS camera (Hamamatsu, Shizuoka Prefecture, Japan), a
623 60x oil immersion objective (UPLAPO OHR; NA 1.49; refractive index 1.518; working distance
624 100 µm), and standard excitation and emission filter sets and lasers were used for all
625 fluorophores. The microscope system was controlled by the CellSens acquisition software
626 (Evident Scientific, Tokyo, Japan). For all live-cell imaging, cells were maintained in DMEM free
627 of phenol red in a Chamlide microscope-mounted chamber at 37°C and 5% CO_2. For z-stack
628 imaging, 20-50 images were acquired with an interplanar distance of 0.2 to 0.6 µm, where
629 origin was set to the centre of the cell. For timelapse obtained for ER and lysosome dynamics
630 and EB1-GFP dynamics, frames were acquired every 0.25 s for 1 min. For timelapse obtained for
631 ER-hitchhiking, frames were acquired every 0.3 s for 1 min.
632

633 *ER and lysosome morphology analysis*

634 Image analysis was conducted using Volocity and Fiji software. ER morphology analysis was
635 conducted on Volocity using an ER protocol designed to provide skeletal length measurements
636 through the thinning (or skeletonizing) of the ER until only a single-voxel-wide-line remains
637 (Arganda-Carreras et al., 2010; Schindelin et al., 2012). The protocol then counts the number of
638 voxels along the path and provides information such as skeletal length, curvature, branching
639 and fragmentation. Further ER morphology and fluorescent ER-protein distribution, analyses
640 were completed using a semi-automated junction analysis plug-in for Fiji provided by Spits *et al*
641 *(2021)* from the Leiden University Medical Centre in the Netherlands. This plug-in was based on
642 the analyze skeleton feature on Fiji where an ER mask is initially created and the skeleton
643 representation is analyzed for the number of junctions and branches (Spits et al., 2021).
644 Lysosome morphology analysis was done on Volocity using a "Measure Objects" protocol
645 designed to provide voxel/pixel count, volume and area, and total number measurements for
646 the entire cell (Hipolito et al., 2019; Saffi et al., 2021).

647

648 *ER and lysosome dynamics analysis*

649 ER dynamics were analyzed using a membrane displacement analysis macro for Fiji also
650 provided by *Spits et al (2021)* that analyzed mobile ER fractions based on #pixels/frame ranging
651 from 0-9. This method is largely based on optical flow analysis which compares corresponding
652 areas in two frames and generates a map that depicts the frame-to-frame movement of specific
653 image areas. The extent of movement is reflected by the change in pixel color intensity
654 between each frame (Spits et al., 2021). Seven separate 60-pixel x 60-pixel regions of interest

655 were randomly selected in a clockwise manner targeting both peripheral and perinuclear ER for
656 one single cell per field of view for seven cells and the mobile ER fractions were determined.
657 We then binned movement into three categories of change (0-3 #pixels/frame), (4-7
658 #pixels/frame) and (8-9 #pixels/frame) to define low-, intermediate-, and rapid-movement.

659 Lysosome dynamics were analyzed using Single Particle Tracking analysis for Fiji, which
660 analyzed lysosome dynamics upon PIKfyve inhibition using time-lapse images acquired every
661 0.25 s for 1 min. Default settings were kept with the LoG detector (Laplacian of Gaussian). In
662 vehicle-treated cells, the diameter of the lysosome was set to 1.5 µm with a quality threshold of
663 500. A uniform color was selected for color spots. The simple LAP Tracker was selected with the
664 linking max distance set to 7 µm, the gap-closing distance set to 5 µm, and the gap closing max
665 frame set to 2 µm. A track index was generated, and the following parameters were extracted:
666 total distance travelled, mean speed, and overall track displacement. In PIKfyve inhibited cells,
667 the same process was followed with the exception that the diameter of the lysosome was set to
668 2 µm with a quality threshold of 250; and both the linking max distance and gap-closing max
669 distance were set to 5 µm. Lysosome motility was also shown using a "Reslice" protocol in Fiji
670 to create Kymographs between conditions, where a segmented line was drawn along the x-axis
671 of the cell randomly, with a line width of 2 pixels; generating a space-time projection displaying
672 spatial position (x-axis) versus time (y-axis).

673 The frequency of ER-hitchhiking events upon PIKfyve inhibition was analyzed using
674 Time-lapse analysis acquired every 0.25 s for 1 min. Cells post-treatment were analyzed to
675 determine the number of ER-hitchhiking events for multiple, randomized (100 μm^2) regions of
676 interest (ROI). To quantify the number of events, Fiji software was utilized to select ROIs based

677 on available ER periphery with co-migrating lysosomes. A positive hitchhiking event was
678 identified if the lysosome localized with the tip of a growing ER tubule, initiated movement, co-
679 travelled with the ER tubule, and "dropped it off" at another independent ER tubule.
680 Hitchhiking events were tracked and identified qualitatively by eye.
681
682 *Lysosome distribution analysis*
683 To determine the change in lysosome distribution, Shell analysis on Fiji software was utilized.
684 Using the Freehand Selection Tool on Fiji, the cell was outlined to create a "total cell" ROI. This
685 was followed by using the Enlarge Tool on Fiji to create a shell by shrinking the "total cell" ROI
686 by 30-50 pixels to create a second layer of shell. This process was repeated to create a third and
687 fourth layer of shell. The raw integrated density was calculated for each shell independently to
688 determine the sum of the values of pixel intensities in the respective shell. The raw integrated
689 density of the innermost shell as a fraction of the "total cell" ROI was calculated and compared
690 to the outermost shell as a fraction of the "total cell" ROI.
691
692 *3D Image Reconstruction*
693 Three-dimensional (3D) image reconstruction was performed using Imaris Software (V9.5,
694 Bitplane, Oxford Instruments). Raw z-stack images (plane thickness: 0.2 µm) were acquired
695 using a ReSCAN Confocal Microscope (previously explained) and imported into Imaris for
696 analysis. Prior to reconstruction, image stacks were subjected to background subtraction
697 preprocessing, with a rolling ball background subtraction of 50 pixels applied across all images
698 and conditions using Fiji software. Within Imaris, 3D volumes were generated using the Surpass

699 Mode, and surfaces were rendered using the Surface or Volume modules, with thresholds set
700 manually based on signal intensity. Reconstruction parameters, including smoothing and
701 thresholding method were consistently applied across all samples to ensure comparability. For
702 visualization, coloring was applied to distinguished channels representing lysosomes (magenta)
703 and protrudin (gray).
704
705 *Recombinant protein expression and purification*
706 GST-fused RILP-C33 (truncated mutant) and GST-fused empty vectors (ampicillin resistant) were
707 expressed in BL21 competent cells, grown at 37 ºC and shaking at 200 rpm over-night . Cells
708 were cultured until the OD_{600} reached 0.6. After treatment with 1 µM isopropyl-ß-D-
709 thiogalactoside (IPTG) for 4 h at 30 ºC and shaking at 200 rpm, the induced recombinant GST-
710 RILP-C33 and GST proteins were centrifuged at 4 ºC for 30 minutes at 5000 xg, with the
711 supernatant discarded and pellet resuspended in 1X bacterial lysis buffer (50 mM Tris, 150 mM
712 NaCl, 10 mM β-mercaptoethanol, pH 7.5 with protease inhibitor cocktail (Sigma-Aldrich). The
713 bacterial lysates were then homogenized using a EmulsiFlex-C3 pressure homogenizer
714 (AVESTIN, Canada). Once homogenized, the recombinant GST-RILP-C33 and GST- lysates were
715 centrifuged at 4 ºC for 30 minutes at 5000 xg, pelleted, and the supernatant was incubated with
716 50% glutathione-Sepharose 4B bead resuspension made following manufacturer's instructions
717 (Millipore Sigma, G317-0756-01) at a dilution of 1:50 (beads to bacterial lysate supernatant,
718 respectively) for 2 h at 4 ºC with gentle shaking. The samples were then centrifuged at 4 ºC for
719 5 minutes at 5000 xg, pelleted, supernatant discarded, and pellet resuspended in 1X bacterial

720 lysis buffer. The samples were analyzed by western blotting to confirm protein expression and
721 purification.
722
723 *Affinity precipitation of GTP-bound Rab7*
724 HeLa cells were pre-treated with either vehicle control (DMSO), apilimod, or YM-201636 and
725 lysed in 700 µL modified- 1X RIPA Buffer (25 mM Tris HCl, 150 mM NaCl, 1% TritonX-100, 1% Na
726 deoxychlorate, pH 7.4 with protease inhibitor cocktail (Sigma-Aldrich)). Cells were then
727 incubated on ice for 30 minutes, collected into clean microcentrifuge tubes and centrifuged at
728 4°C for 5 minutes at 3,000 xg. Prior to centrifugation, 10% of each lysate sample was collected
729 reserved as an input control. These input samples were also centrifuged at 4°C for 5 minutes at
730 3,000 xg and subsequently mixed with a 1:1 ratio of 2X Laemmli Sample Buffer (0.5 M Tris, pH
731 6.8, glycerol and 10% sodium dodecyl sulfate (SDS), 1:10 β-mercaptoethanol). Recombinant
732 RILP-C33 and GST bound to glutathione-Sepharose 4B beads previously explained were mixed
733 with HeLa cell lysates at a dilution of 1:14 (beads to cell lysate, respectively). These mixtures
734 were incubated for 2 h at 4 ºC with gentle shaking. The samples were then centrifuged at 4°C
735 for 5 minutes at 500 xg, with remaining supernatant discarded. The sample pellets were eluted
736 using modified-1X RIPA Buffer (1:2 ratio of sample to buffer, respectively). The supernatant
737 from each wash was moved to a clean microcentrifuge tube and a 1:1 ratio of 2X Laemmli
738 Sample was added to the samples, boiled at 96°C for 10 minutes and resolved via SDS-PAGE.
739
740 *SDS-PAGE and Western blotting*

741 Following treatment, whole cell lysates were prepared in 200 µL 2x Laemmli Sample Buffer (0.5
742 M Tris, pH 6.8, glycerol and 10% SDS) supplemented with a protease and phosphatase inhibitor
743 cocktail (Complete 1x protease inhibitor (Sigma-Aldrich), Halt phosphatase inhibitor cocktail
744 (ThermoFisher Scientific)). Lysates were heated at 95°C for 10 min, and 10% β-mercaptoethanol
745 and 5% bromophenol blue were added to the cell lysates. Proteins were resolved by Tris-
746 Glycine SDS-PAGE and transferred on to a polyvinylidene difluoride (PVDF) membrane. The
747 PVDF membrane was blocked for 1 h at RT in blocking buffer composed of 5% BSA in 1x final
748 Tris-buffered saline-Tween (TBS-T; 20 nM Tris, 150 mM NaCl, and 0.1% Tween-20) After
749 blocking, membranes were washed and incubated with primary antibody (at designated
750 dilution) overnight at 4°C. Primary antibodies used for western blotting include: rabbit
751 polyclonal antibody against Vac14 (1:1000, SAB4200074, Sigma Aldrich), rabbit polyclonal
752 antibody against protrudin (1:1000, 12680-1-AP, Proteintech), rabbit monoclonal (14C10)
753 antibody against GDPH (1:5000, #2118S, Cell Signaling Technology), rabbit monoclonal (DE3C6)
754 antibody against clathrin (1:5000, #4796s, Cell Signaling Technology), rabbit monoclonal
755 (D95F2) antibody against Rab7 (1:1000, #9367S, Cell Signaling Technology) and rabbit
756 monoclonal antibody against beta-actin (1:5000, #4967, Cell Signaling Technology). After
757 primary incubation, membranes were washed and then subjected to secondary antibody (at
758 designated dilution) incubation for 1 h at RT. After incubation with secondary antibody,
759 membranes were washed and imaged using the Chemi-Doc Imaging System (Bio-Rad). Western
760 blot signals were analyzed and quantified using ImageLab 6.1 (Bio-Rad). Band intensity was
761 quantified by signal integration in an area corresponding to the appropriate band.
762

763 *FKBP-FRB Inducible Dimerization*

764 For inducible FKBP-FRB dimerization experiments, COS-7 cells were seeded at a density of 2.0 x
765 10^4 cells/mL and cultured overnight. For baseline ER morphology analysis (in the absence of
766 FKBP-FRB heterodimerization), cells were transfected with GFP-protrudin$^{WT.}$ Following
767 transfection, cells were washed with PBS and replenished with DMEM. Lysosomes were
768 labelled using Alexa Fluor 546-Dextran, followed by treatment with either 0.02% DMSO
769 (vehicle) or 240 nM apilimod treatment for 2 h. For inducible FKBP-FRB dimerization
770 experiments, COS-7 cells were co-transfected with either protrudin^{WT} or protrudin^{FYVE4A} FKBP-
771 mCherry constructs and iRFP-FRB-Rab7. Following transfection, cells were washed with PBS and
772 replenished with DMEM. Cells were then treated with 1 µM VPS34-In1 for 2 h, or with 100 nM
773 Rapamycin for 15 min, or rapamycin and VPS34-IN1 prior to imaging. Live-cell imaging was
774 performed with z-stacks acquired (plane thickness = 0.2 µm).

775

776 *Statistical Analysis*

777 All experiments were performed at least three independent times with the specific total
778 number indicated in the respective figure legends along with sample size. The mean and
779 measure of variation such as standard deviation (STD) or standard error of the mean (SEM) are
780 indicated. When shown, violin plots indicate range, followed dotted lines to display 25-75%
781 percentile, the dashed line indicates median of the sampled populations. Sample means of
782 independent experiments are shown and colour coded to match the independent experiment
783 across conditions. All experimental conditions were statistically analyzed with the actual tests
784 disclosed in the respective figure legend. Unless data was normalized, sampling was assumed to

785 be normally distributed. As such, data was typically assessed with paired Student's t-test when
786 comparing two populations, with a repeated-measures one-way ANOVA for three or more
787 samples with one parameter, repeated-measures two-way ANOVA when two parameters were
788 considered, or repeated-measures three-way ANOVA when three parameters were considered.
789 The Geisser-Greenhouse correction was applied. Post-hoc tests were employed based on
790 assumptions and comparisons as recommended by GraphPad Prism and disclosed in the
791 respective figure legends when comparing multiple conditions in non-normalized controls.
792 ANOVA tests were coupled to Dunnett's Multiple Comparison Test for one-way analysis and
793 Tukey's multiple comparison test for two-way analysis, to analyze pairwise conditions. Here, we
794 disclose all p values for greater transparency, while we employ the standard $p<0.05$ to support
795 a statistical difference between populations, we view $p<0.1$ as indicative of a difference and
796 $p<0.01$ as very high confidence of a difference.

797

798 **References**

799 Abrisch, R.G., S.C. Gumbin, B.T. Wisniewski, L.L. Lackner, and G.K. Voeltz. 2020. Fission and
800 fusion machineries converge at ER contact sites to regulate mitochondrial morphology.
801 *Journal of Cell Biology*. 219. doi:10.1083/JCB.201911122.

802 Allison, R., J.R. Edgar, G. Pearson, T. Rizo, T. Newton, S. Günther, F. Berner, J. Hague, J.W.
803 Connell, J. Winkler, J. Lippincott-Schwartz, C. Beetz, B. Winner, and E. Reid. 2017.
804 Defects in ER–endosome contacts impact lysosome function in hereditary spastic
805 paraplegia. *The Journal of Cell Biology*. jcb.201609033. doi:10.1083/jcb.201609033.

806 Arganda-Carreras, I., R. Fernández-González, A. Muñoz-Barrutia, and C. Ortiz-De-Solorzano.
807 2010. 3D reconstruction of histological sections: Application to mammary gland tissue.
808 *Microscopy Research and Technique*. 73:1019–1029. doi:10.1002/jemt.20829.

809 Babu, S., K.A. Nicholson, J.D. Rothstein, A. Swenson, P.J. Sampognaro, P. Pant, E.A. Macklin, S.
810 Spruill, S. Paganoni, T.F. Gendron, M. Prudencio, L. Petrucelli, D. Nix, S. Landrette, E.
811 Nkrumah, K. Fandrick, J. Edwards, and P.R. Young. 2024. Apilimod dimesylate in C9orf72

812 amyotrophic lateral sclerosis: a randomized phase 2a clinical trial. *Brain*. 147:2998–
813 3008. doi:10.1093/brain/awae109.

814 Ballabio, A., and J.S. Bonifacino. 2020. Lysosomes as dynamic regulators of cell and organismal
815 homeostasis. *Nat Rev Mol Cell Biol*. 21:101–118. doi:10.1038/s41580-019-0185-4.

816 Bao, Y., Y. Qiao, J.E. Choi, Y. Zhang, R. Mannan, C. Cheng, T. He, Y. Zheng, J. Yu, M. Gondal, G.
817 Cruz, S. Grove, X. Cao, F. Su, R. Wang, Y. Chang, I. Kryczek, M. Cieslik, M.D. Green, W.
818 Zou, and A.M. Chinnaiyan. 2023. Targeting the lipid kinase PIKfyve upregulates surface
819 expression of MHC class I to augment cancer immunotherapy. *Proc Natl Acad Sci U S A*.
820 120:e2314416120. doi:10.1073/pnas.2314416120.

821 Bissig, C., I. Hurbain, G. Raposo, and G. van Niel. 2017. PIKfyve activity regulates reformation of
822 terminal storage lysosomes from endolysosomes. *Traffic*. 18:747–757.
823 doi:10.1111/tra.12525.

824 Bonet-Ponce, L., and M.R. Cookson. 2022. The endoplasmic reticulum contributes to lysosomal
825 tubulation/sorting driven by LRRK2. *Mol Biol Cell*. 33:ar124. doi:10.1091/mbc.E22-04-
826 0139.

827 Botelho, R.J. 2009. Changing phosphoinositides "on the fly": How trafficking vesicles avoid an
828 identity crisis. *BioEssays*. 31. doi:10.1002/bies.200900060.

829 Botelho, R.J., J.A. Efe, D. Teis, and S.D. Emr. 2008. Assembly of a Fab1 phosphoinositide kinase
830 signaling complex requires the Fig4 phosphoinositide phosphatase. *Mol Biol Cell*.
831 19:4273–4286. doi:10.1091/mbc.e08-04-0405.

832 Bucci, C., R.G. Parton, I.H. Mather, H. Stunnenberg, K. Simons, B. Hoflack, and M. Zerial. 1992.
833 The small GTPase rab5 functions as a regulatory factor in the early endocytic pathway.
834 *Cell*. 70:715–728. doi:10.1016/0092-8674(92)90306-W.

835 Cabukusta, B., and J. Neefjes. 2018. Mechanisms of lysosomal positioning and movement.
836 *Traffic*. 19:761–769. doi:10.1111/tra.12587.

837 Cai, S., Y. Wu, A. Guillén-Samander, W. Hancock-Cerutti, J. Liu, and P. De Camilli. 2022. In situ
838 architecture of the lipid transport protein VPS13C at ER-lysosome membrane contacts.
839 *Proc Natl Acad Sci U S A*. 119:e2203769119. doi:10.1073/pnas.2203769119.

840 Cai, X., Y. Xu, A.K. Cheung, R.C. Tomlinson, A. Alcázar-Román, L. Murphy, A. Billich, B. Zhang, Y.
841 Feng, M. Klumpp, J.-M. Rondeau, A.N. Fazal, C.J. Wilson, V. Myer, G. Joberty, T.
842 Bouwmeester, M.A. Labow, P.M. Finan, J.A. Porter, H.L. Ploegh, D. Baird, P. De Camilli,
843 J.A. Tallarico, and Q. Huang. 2013. PIKfyve, a class III PI kinase, is the target of the small
844 molecular IL-12/IL-23 inhibitor apilimod and a player in Toll-like receptor signaling.
845 *Chemistry & biology*. 20:912–21. doi:10.1016/j.chembiol.2013.05.010.

846 Cantalupo, G., P. Alifano, V. Roberti, C.B. Bruni, and C. Bucci. 2001. Rab-interacting lysosomal
847 protein (RILP): The Rab7 effector required for transport to lysosomes. *EMBO Journal*.
848 20:683–693. doi:10.1093/emboj/20.4.683.

849 Chang, J., S. Lee, and C. Blackstone. 2013. Protrudin binds atlastins and endoplasmic reticulum-
850 shaping proteins and regulates network formation. *Proceedings of the National*
851 *Academy of Sciences*. 110:14954–14959. doi:10.1073/pnas.1307391110.

852 Chavrier, P., R.G. Parton, H.P. Hauri, K. Simons, and M. Zerial. 1990. Localization of low
853 molecular weight GTP binding proteins to exocytic and endocytic compartments. *Cell*.
854 62:317–329. doi:10.1016/0092-8674(90)90369-p.

855 Chen, X., C. Shi, M. He, S. Xiong, and X. Xia. 2023. Endoplasmic reticulum stress: molecular
856 mechanism and therapeutic targets. *Sig Transduct Target Ther*. 8:352.
857 doi:10.1038/s41392-023-01570-w.

858 Cheng, C., J. Hu, R. Mannan, T. He, R. Bhattacharyya, B. Magnuson, J.P. Wisniewski, S. Peters,
859 S.A. Karim, D.J. MacLean, H. Karabürk, L. Zhang, N.J. Rossiter, Y. Zheng, L. Xiao, C. Li, D.
860 Awad, S. Mahapatra, Y. Bao, Y. Zhang, X. Cao, Z. Wang, R. Mehra, P. Morlacchi, V. Sahai,
861 M. Pasca di Magliano, Y.M. Shah, L.S. Weisman, J.P. Morton, K. Ding, Y. Qiao, C.A.
862 Lyssiotis, and A.M. Chinnaiyan. 2025. Targeting PIKfyve-driven lipid metabolism in
863 pancreatic cancer. *Nature*. doi:10.1038/s41586-025-08917-z.

864 Chertkova, A.O., M. Mastop, M. Postma, N. van Bommel, S. van der Niet, K.L. Batenburg, L.
865 Joosen, T.W.J. Gadella, Y. Okada, and J. Goedhart. 2020. Robust and Bright Genetically
866 Encoded Fluorescent Markers for Highlighting Structures and Compartments in
867 Mammalian Cells. 160374. doi:10.1101/160374.

868 Chow, C.Y., Y. Zhang, J.J. Dowling, N. Jin, M. Adamska, K. Shiga, K. Szigeti, M.E. Shy, J. Li, X.
869 Zhang, J.R. Lupski, L.S. Weisman, and M.H. Meisler. 2007. Mutation of FIG4 causes
870 neurodegeneration in the pale tremor mouse and patients with CMT4J. *Nature*. 448:68–
871 72. doi:10.1038/nature05876.

872 Choy, C.H., G. Saffi, M.A. Gray, C. Wallace, R.M. Dayam, Z.Y.A. Ou, G. Lenk, R. Puertollano, S.C.
873 Watkins, and R.J. Botelho. 2018. Lysosome enlargement during inhibition of the lipid
874 kinase PIKfyve proceeds through lysosome coalescence. *Journal of Cell Science*.
875 131:jcs213587. doi:10.1242/JCS.213587.

876 Dong, X., D. Shen, X. Wang, T. Dawson, X. Li, Q. Zhang, X. Cheng, Y. Zhang, L.S. Weisman, M.
877 Delling, and H. Xu. 2010. PI(3,5)P(2) controls membrane trafficking by direct activation
878 of mucolipin Ca(2+) release channels in the endolysosome. *Nature communications*.
879 1:38. doi:10.1038/ncomms1037.

880 Du, Y., W. Chang, L. Gao, L. Deng, and W.-K. Ji. 2023. Tex2 is required for lysosomal functions at
881 TMEM55-dependent ER membrane contact sites. *J Cell Biol*. 222:e202205133.
882 doi:10.1083/jcb.202205133.

883 Ferris, A.L., J.C. Brown, R.D. Park, and B. Storrie. 1987. Chinese hamster ovary cell lysosomes
884 rapidly exchange contents. *J Cell Biol*. 105:2703–2712. doi:10.1083/jcb.105.6.2703.

885 Friedman, J.R., J.R. DiBenedetto, M. West, A.A. Rowland, and G.K. Voeltz. 2013. Endoplasmic
886 reticulum-endosome contact increases as endosomes traffic and mature. *Molecular*
887 *Biology of the Cell*. 24:1030–1040. doi:10.1091/mbc.E12-10-0733.

888 Friedman, J.R., L.L. Lackner, M. West, J.R. DiBenedetto, J. Nunnari, and G.K. Voeltz. 2011. ER
889 tubules mark sites of mitochondrial division. *Science*. 334:358–362.
890 doi:10.1126/science.1207385.

891 Gao, Y., J. Xiong, Q.-Z. Chu, and W.-K. Ji. 2022. PDZD8-mediated lipid transfer at contacts
892 between the ER and late endosomes/lysosomes is required for neurite outgrowth. *J Cell*
893 *Sci*. 135:jcs255026. doi:10.1242/jcs.255026.

894 Gopaldass, N., B. Fauvet, H. Lashuel, A. Roux, and A. Mayer. 2017. Membrane scission driven by
895 the PROPPIN Atg18. *The EMBO Journal*. 36:e201796859. doi:10.15252/embj.201796859.

896 Goyal, U., and C. Blackstone. 2013. Untangling the web: mechanisms underlying ER network
897 formation. *Biochim Biophys Acta*. 1833:2492–2498. doi:10.1016/j.bbamcr.2013.04.009.

898 Grigoriev, I., S.M. Gouveia, B. van der Vaart, J. Demmers, J.T. Smyth, S. Honnappa, D. Splinter,
899 M.O. Steinmetz, J.W. Putney, C.C. Hoogenraad, and A. Akhmanova. 2008. STIM1 is a MT-
900 plus-end-tracking protein involved in remodeling of the ER. *Curr Biol*. 18:177–182.
901 doi:10.1016/j.cub.2007.12.050.

902 Guardia, C.M., G.G. Farías, R. Jia, J. Pu, and J.S. Bonifacino. 2016. BORC Functions Upstream of
903 Kinesins 1 and 3 to Coordinate Regional Movement of Lysosomes along Different
904 Microtubule Tracks. *Cell reports*. 17:1950–1961. doi:10.1016/j.celrep.2016.10.062.

905 Guimaraes, S.C., M. Schuster, E. Bielska, G. Dagdas, S. Kilaru, B.R.A. Meadows, M. Schrader, and
906 G. Steinberg. 2015. Peroxisomes, lipid droplets, and endoplasmic reticulum "hitchhike"
907 on motile early endosomes. *J Cell Biol*. 211:945–954. doi:10.1083/jcb.201505086.

908 Guo, Y., D. Li, S. Zhang, Y. Yang, J.-J. Liu, X. Wang, C. Liu, D.E. Milkie, R.P. Moore, U.S. Tulu, D.P.
909 Kiehart, J. Hu, J. Lippincott-Schwartz, E. Betzig, and D. Li. 2018. Visualizing Intracellular
910 Organelle and Cytoskeletal Interactions at Nanoscale Resolution on Millisecond
911 Timescales. *Cell*. 175:1430-1442.e17. doi:10.1016/j.cell.2018.09.057.

912 Hammond, G.R.V., M.P. Machner, and T. Balla. 2014. A novel probe for phosphatidylinositol 4-
913 phosphate reveals multiple pools beyond the Golgi. *J Cell Biol*. 205:113–126.
914 doi:10.1083/jcb.201312072.

915 Hashimoto, Y., M. Shirane, F. Matsuzaki, S. Saita, T. Ohnishi, and K.I. Nakayama. 2014. Protrudin
916 regulates endoplasmic reticulum morphology and function associated with the
917 pathogenesis of hereditary spastic paraplegia. *J Biol Chem*. 289:12946–12961.
918 doi:10.1074/jbc.M113.528687.

919 Hipolito, V.E.B., J.A. Diaz, K.V. Tandoc, C. Oertlin, J. Ristau, N. Chauhan, A. Saric, S. Mclaughlan,
920 O. Larsson, I. Topisirovic, and R.J. Botelho. 2019. Enhanced translation expands the
921 endo-lysosome size and promotes antigen presentation during phagocyte activation.
922 *PLoS Biol*. 17:e3000535. doi:10.1371/journal.pbio.3000535.

923 Hong, N.H., A. Qi, and A.M. Weaver. 2015. PI(3,5)P2 controls endosomal branched actin
924 dynamics by regulating cortactin-Actin interactions. *Journal of Cell Biology*. 210:753–
925 769. doi:10.1083/jcb.201412127.

926 Hu, J., Y. Shibata, P.-P. Zhu, C. Voss, N. Rismanchi, W.A. Prinz, T.A. Rapoport, and C. Blackstone.
927 2009. A class of dynamin-like GTPases involved in the generation of the tubular ER
928 network. *Cell*. 138:549–561. doi:10.1016/j.cell.2009.05.025.

929 Ikonomov, O.C., D. Sbrissa, K. Delvecchio, Y. Xie, J.-P.P.J.-P. Jin, D. Rappolee, and A. Shisheva.
930 2011. The phosphoinositide kinase PIKfyve is vital in early embryonic development:
931 preimplantation lethality of PIKfyve-/- embryos but normality of PIKfyve+/- mice.
932 *Journal of Biological Chemistry*. 286:13404–13413. doi:10.1074/jbc.M111.222364.

933 Ikonomov, O.C., D. Sbrissa, and A. Shisheva. 2001. Mammalian cell morphology and endocytic
934 membrane homeostasis require enzymatically active phosphoinositide 5-kinase PIKfyve.
935 *The Journal of biological chemistry*. 276:26141–7. doi:10.1074/jbc.M101722200.

936 Inpanathan, S., and R.J. Botelho. 2019. The Lysosome Signaling Platform: Adapting With the
937 Times. *Frontiers in Cell and Developmental Biology*. 7:113. doi:10.3389/fcell.2019.00113.

938 Jin, N., C.Y. Chow, L. Liu, S.N. Zolov, R. Bronson, M. Davisson, J.L. Petersen, Y. Zhang, S. Park, J.E.
939 Duex, D. Goldowitz, M.H. Meisler, and L.S. Weisman. 2008. VAC14 nucleates a protein
940 complex essential for the acute interconversion of PI3P and PI(3,5)P(2) in yeast and
941 mouse. *The EMBO journal*. 27:3221–34. doi:10.1038/emboj.2008.248.

942 Jongsma, M.L.M., N. Bakker, L.M. Voortman, R.I. Koning, E. Bos, J.J.L.L. Akkermans, L. Janssen,
943 and J. Neefjes. 2024. Systems mapping of bidirectional endosomal transport through the
944 crowded cell. *Current Biology*. 34:4476-4494.e11. doi:10.1016/j.cub.2024.08.026.

945 Jongsma, M.L.M., I. Berlin, R.H.M. Wijdeven, L. Janssen, G.M.C. Janssen, M.A. Garstka, H.
946 Janssen, M. Mensink, P.A. van Veelen, R.M. Spaapen, and J. Neefjes. 2016. An ER-
947 Associated Pathway Defines Endosomal Architecture for Controlled Cargo Transport.
948 *Cell*. 166:152–166. doi:10.1016/j.cell.2016.05.078.

949 Kang, Y.-L., Y. Chou, P.W. Rothlauf, Z. Liu, T.K. Soh, D. Cureton, J.B. Case, R.E. Chen, M.S.
950 Diamond, S.P.J. Whelan, and T. Kirchhausen. 2020. Inhibition of PIKfyve kinase prevents

951 infection by Zaire ebolavirus and SARS-CoV-2. *Proceedings of the National Academy of*
952 *Sciences*. 202007837. doi:10.1073/pnas.2007837117.

953 Keren-Kaplan, T., A. Sarić, S. Ghosh, C.D. Williamson, R. Jia, Y. Li, and J.S. Bonifacino. 2022.
954 RUFY3 and RUFY4 are ARL8 effectors that promote coupling of endolysosomes to
955 dynein-dynactin. *Nature Communications*. 13:1506. doi:10.1038/s41467-022-28952-y.

956 Khatter, D., V.B. Raina, D. Dwivedi, A. Sindhwani, S. Bahl, and M. Sharma. 2015. The small
957 GTPase Arl8b regulates assembly of the mammalian HOPS complex on lysosomes.
958 *Journal of cell science*. 128:1746–61. doi:10.1242/jcs.162651.

959 Kumar, G., P. Chawla, N. Dhiman, S. Chadha, S. Sharma, K. Sethi, M. Sharma, and A. Tuli. 2022.
960 RUFY3 links Arl8b and JIP4-Dynein complex to regulate lysosome size and positioning.
961 *Nature Communications*. 13:1540. doi:10.1038/s41467-022-29077-y.

962 Langley, A., S. Abeling-Wang, E. Wagner, and J. Salogiannis. 2025. Movement of the
963 endoplasmic reticulum is driven by multiple classes of vesicles marked by Rab-GTPases.
964 *Mol Biol Cell*. 36:ar9. doi:10.1091/mbc.E24-04-0197.

965 de Lartigue, J., H. Polson, M. Feldman, K. Shokat, S.A. Tooze, S. Urbé, and M.J. Clague. 2009.
966 PIKfyve regulation of endosome-linked pathways. *Traffic*. 10:883–893.
967 doi:10.1111/j.1600-0854.2009.00915.x.

968 Leray, X., J.K. Hilton, K. Nwangwu, A. Becerril, V. Mikusevic, G. Fitzgerald, A. Amin, M.R. Weston,
969 and J.A. Mindell. 2022. Tonic inhibition of the chloride/proton antiporter ClC-7 by
970 PI(3,5)P2 is crucial for lysosomal pH maintenance. *eLife*. 11:e74136.
971 doi:10.7554/eLife.74136.

972 Li, L., X. Liu, S. Yang, M. Li, Y. Wu, S. Hu, W. Wang, A. Jiang, Q. Zhang, J. Zhang, X. Ma, J. Hu, Q.
973 Zhao, Y. Liu, D. Li, J. Hu, C. Yang, W. Feng, and X. Wang. 2024. The HEAT repeat protein
974 HPO-27 is a lysosome fission factor. *Nature*. 628:630–638. doi:10.1038/s41586-024-
975 07249-8.

976 Li, X., N. Rydzewski, A. Hider, X. Zhang, J. Yang, W. Wang, Q. Gao, X. Cheng, and H. Xu. 2016. A
977 molecular mechanism to regulate lysosome motility for lysosome positioning and
978 tubulation. *Nat Cell Biol*. 18:404–417. doi:10.1038/ncb3324.

979 Lu, M., F.W. van Tartwijk, J.Q. Lin, W. Nijenhuis, P. Parutto, M. Fantham, C.N. Christensen, E.
980 Avezov, C.E. Holt, A. Tunnacliffe, D. Holcman, L. Kapitein, G.S.K. Schierle, and C.F.
981 Kaminski. 2020. The structure and global distribution of the endoplasmic reticulum
982 network are actively regulated by lysosomes. *Sci Adv*. 6:eabc7209.
983 doi:10.1126/sciadv.abc7209.

984 Luzio, J.P., P.R. Pryor, and N.A. Bright. 2007. Lysosomes: fusion and function. *Nature reviews.*
985 *Molecular cell biology*. 8:622–632. doi:10.1038/nrm2217.

986 Mas, C., S.J. Norwood, A. Bugarcic, G. Kinna, N. Leneva, O. Kovtun, R. Ghai, L.E. Ona Yanez, J.L.
987 Davis, R.D. Teasdale, and B.M. Collins. 2014. Structural basis for different
988 phosphoinositide specificities of the PX domains of sorting nexins regulating G-protein
989 signaling. *J Biol Chem*. 289:28554–28568. doi:10.1074/jbc.M114.595959.

990 Matsuzaki, F., M. Shirane, M. Matsumoto, and K.I. Nakayama. 2011. Protrudin serves as an
991 adaptor molecule that connects KIF5 and its cargoes in vesicular transport during
992 process formation. *Mol Biol Cell*. 22:4602–4620. doi:10.1091/mbc.E11-01-0068.

993 Min, S.H., A. Suzuki, T.J. Stalker, L. Zhao, Y. Wang, C. McKennan, M.J. Riese, J.F. Guzman, S.
994 Zhang, L. Lian, R. Joshi, R. Meng, S.H. Seeholzer, J.K. Choi, G. Koretzky, M.S. Marks, and
995 C.S. Abrams. 2014. Loss of PIKfyve in platelets causes a lysosomal disease leading to
996 inflammation and thrombosis in mice. *Nature communications*. 5:4691.
997 doi:10.1038/ncomms5691.

998 Min, S.H., A. Suzuki, L. Weaver, J. Guzman, Y. Chung, H. Jin, F. Gonzalez, C. Trasorras, L. Zhao,
999 L.A. Spruce, S.H. Seeholzer, E.M. Behrens, and C.S. Abrams. 2019. PIKfyve Deficiency in
1000 Myeloid Cells Impairs Lysosomal Homeostasis in Macrophages and Promotes Systemic
1001 Inflammation in Mice. *Molecular and Cellular Biology*. 39. doi:10.1128/mcb.00158-19.

1002 Ohkuma, S., and B. Poole. 1978. Fluorescence probe measurement of the intralysosomal pH in
1003 living cells and the perturbation of pH by various agents. *Proc Natl Acad Sci U S A*.
1004 75:3327–3331. doi:10.1073/pnas.75.7.3327.

1005 Pankiv, S., E. a. Alemu, A. Brech, J.-A.A. Bruun, T. Lamark, A. Øvervatn, G. Bjørkøy, T. Johansen,
1006 A. Overvatn, G. Bjørkøy, and T. Johansen. 2010. FYCO1 is a Rab7 effector that binds to
1007 LC3 and PI3P to mediate microtubule plus end - Directed vesicle transport. *Journal of*
1008 *Cell Biology*. 188:253–269. doi:10.1083/jcb.200907015.

1009 Pedersen, N.M., E.M. Wenzel, L. Wang, S. Antoine, P. Chavrier, H. Stenmark, and C. Raiborg.
1010 2020. Protrudin-mediated ER–endosome contact sites promote MT1-MMP exocytosis
1011 and cell invasion. *Journal of Cell Biology*. 219:e202003063. doi:10.1083/jcb.202003063.

1012 Prado, D.S., R.T. Cattley, A.B. Sonego, P. Sutariya, S. Wu, M. Lee, W.C. Boggess, M.J. Shlomchik,
1013 and W.F. Hawse. 2025. The phospholipid kinase PIKFYVE is essential for Th17
1014 differentiation. *J Exp Med*. 222:e20240625. doi:10.1084/jem.20240625.

1015 Raiborg, C., E.M. Wenzel, N.M. Pedersen, H. Olsvik, K.O. Schink, S.W. Schultz, M. Vietri, V. Nisi,
1016 C. Bucci, A. Brech, T. Johansen, and H. Stenmark. 2015a. Repeated ER-endosome
1017 contacts promote endosome translocation and neurite outgrowth. *Nature*. 520:234–8.
1018 doi:10.1038/nature14359.

1019 Raiborg, C., E.M. Wenzel, and H. Stenmark. 2015b. ER –endosome contact sites: molecular
1020 compositions and functions. *The EMBO Journal*. 34:1848–1858.
1021 doi:10.15252/embj.201591481.

1022 Rizalar, F.S., M.T. Lucht, A. Petzoldt, S. Kong, J. Sun, J.H. Vines, N.S. Telugu, S. Diecke, T. Kaas, T.
1023 Bullmann, C. Schmied, D. Löwe, J.S. King, W. Cho, S. Hallermann, D. Puchkov, S.J. Sigrist,
1024 and V. Haucke. 2023. Phosphatidylinositol 3,5-bisphosphate facilitates axonal vesicle
1025 transport and presynapse assembly. *Science*. 382:223–230.
1026 doi:10.1126/science.adg1075.

1027 Rodríguez-García, R., V.A. Volkov, C.-Y. Chen, E.A. Katrukha, N. Olieric, A. Aher, I. Grigoriev, M.P.
1028 López, M.O. Steinmetz, L.C. Kapitein, G. Koenderink, M. Dogterom, and A. Akhmanova.
1029 2020. Mechanisms of Motor-Independent Membrane Remodeling Driven by Dynamic
1030 Microtubules. *Current Biology*. 30:972-987.e12. doi:10.1016/j.cub.2020.01.036.

1031 Rowland, A.A., P.J. Chitwood, M.J. Phillips, and G.K. Voeltz. 2014. ER contact sites define the
1032 position and timing of endosome fission. *Cell*. 159:1027–1041.
1033 doi:10.1016/j.cell.2014.10.023.

1034 Rudnik, S., S. Heybrock, E. Coyaud, Z. Xu, D. Neculai, B. Raught, V. Oorschot, C. Heus, J.
1035 Klumperman, and P. Saftig. 2024. The lysosomal lipid transporter LIMP-2 is part of
1036 lysosome-ER STARD3-VAPB-dependent contact sites. *J Cell Sci*. 137:jcs261810.
1037 doi:10.1242/jcs.261810.

1038 Saffi, G.T., and R.J. Botelho. 2019. Lysosome Fission: Planning for an Exit. *Trends in Cell Biology*.
1039 29:635–646. doi:10.1016/j.tcb.2019.05.003.

1040 Saffi, G.T., E. Tang, S. Mamand, S. Inpanathan, A. Fountain, L. Salmena, and R.J. Botelho. 2021.
1041 Reactive oxygen species prevent lysosome coalescence during PIKfyve inhibition. *PLoS*
1042 *ONE*. 16. doi:10.1371/journal.pone.0259313.

1043 Saita, S., M. Shirane, T. Natume, S.-I. Iemura, and K.I. Nakayama. 2009. Promotion of neurite
1044 extension by protrudin requires its interaction with vesicle-associated membrane
1045 protein-associated protein. *J Biol Chem*. 284:13766–13777.
1046 doi:10.1074/jbc.M807938200.

1047 Saric, A., S.A. Freeman, C.D. Williamson, M. Jarnik, C.M. Guardia, M.S. Fernandopulle, D.C.
1048 Gershlick, and J.S. Bonifacino. 2021. SNX19 restricts endolysosome motility through
1049 contacts with the endoplasmic reticulum. *Nat Commun*. 12:4552. doi:10.1038/s41467-
1050 021-24709-1.

1051 Sbrissa, D., O.C. Ikonomov, Z. Fu, T. Ijuin, J. Gruenberg, T. Takenawa, and A. Shisheva. 2007.
1052 Core protein machinery for mammalian phosphatidylinositol 3,5-bisphosphate synthesis
1053 and turnover that regulates the progression of endosomal transport: Novel Sac
1054 phosphatase joins the ArPIKfyve-PIKfyve complex. *Journal of Biological Chemistry*.
1055 282:23878–23891. doi:10.1074/jbc.M611678200.

1056 Sbrissa, D., O.C. Ikonomov, and A. Shisheva. 2002. Phosphatidylinositol 3-phosphate-interacting
1057 domains in PIKfyve. Binding specificity and role in PIKfyve. Endomenbrane localization.
1058 *The Journal of biological chemistry*. 277:6073–9. doi:10.1074/jbc.M110194200.

1059 Schindelin, J., I. Arganda-Carreras, E. Frise, V. Kaynig, M. Longair, T. Pietzsch, S. Preibisch, C.
1060 Rueden, S. Saalfeld, B. Schmid, J.-Y. Tinevez, D.J. White, V. Hartenstein, K. Eliceiri, P.
1061 Tomancak, and A. Cardona. 2012. Fiji: an open-source platform for biological-image
1062 analysis. *Nat Methods*. 9:676–682. doi:10.1038/nmeth.2019.

1063 Sharma, G., C.M. Guardia, A. Roy, A. Vassilev, A. Saric, L.N. Griner, J. Marugan, M. Ferrer, J.S.
1064 Bonifacino, and M.L. DePamphilis. 2019. A family of PIKFYVE inhibitors with therapeutic
1065 potential against autophagy-dependent cancer cells disrupt multiple events in lysosome
1066 homeostasis. *Autophagy*. 15:1694–1718. doi:10.1080/15548627.2019.1586257.

1067 Shibata, Y., T. Shemesh, W.A. Prinz, A.F. Palazzo, M.M. Kozlov, and T.A. Rapoport. 2010.
1068 Mechanisms Determining the Morphology of the Peripheral ER. *Cell*. 143:774–788.
1069 doi:10.1016/j.cell.2010.11.007.

1070 Shibata, Y., C. Voss, J.M. Rist, J. Hu, T.A. Rapoport, W.A. Prinz, and G.K. Voeltz. 2008. The
1071 reticulon and DP1/Yop1p proteins form immobile oligomers in the tubular endoplasmic
1072 reticulum. *J Biol Chem*. 283:18892–18904. doi:10.1074/jbc.M800986200.

1073 Shirane, M., and K.I. Nakayama. 2006. Protrudin induces neurite formation by directional
1074 membrane trafficking. *Science*. 314:818–821. doi:10.1126/science.1134027.

1075 Spits, M., I.T. Heesterbeek, L.M. Voortman, J.J. Akkermans, R.H. Wijdeven, B. Cabukusta, and J.
1076 Neefjes. 2021. Mobile late endosomes modulate peripheral endoplasmic reticulum
1077 network architecture. *EMBO reports*. 22. doi:10.15252/embr.202050815.

1078 Tsuruta, F., E.M. Green, M. Rousset, and R.E. Dolmetsch. 2009. PIKfyve regulates CaV1.2
1079 degradation and prevents excitotoxic cell death. *Journal of Cell Biology*. 187:279–294.
1080 doi:10.1083/jcb.200903028.

1081 Voeltz, G.K., W.A. Prinz, Y. Shibata, J.M. Rist, and T.A. Rapoport. 2006. A class of membrane
1082 proteins shaping the tubular endoplasmic reticulum. *Cell*. 124:573–586.
1083 doi:10.1016/j.cell.2005.11.047.

1084 Voeltz, G.K., E.M. Sawyer, G. Hajnóczky, and W.A. Prinz. 2024. Making the connection: How
1085 membrane contact sites have changed our view of organelle biology. *Cell*. 187:257–270.
1086 doi:10.1016/j.cell.2023.11.040.

1087 Vonderheit, A., and A. Helenius. 2005. Rab7 Associates with Early Endosomes to Mediate
1088 Sorting and Transport of Semliki Forest Virus to Late Endosomes. *PLOS Biology*. 3:e233.
1089 doi:10.1371/journal.pbio.0030233.

Wang, S., H. Tukachinsky, F.B. Romano, and T.A. Rapoport. 2016. Cooperation of the ER-shaping proteins atlastin, lunapark, and reticulons to generate a tubular membrane network. *eLife*. 5:e18605. doi:10.7554/eLife.18605.

Wang, X., X. Zhang, X.-P. Dong, M. Samie, X. Li, X. Cheng, A. Goschka, D. Shen, Y. Zhou, J. Harlow, M.X. Zhu, D.E. Clapham, D. Ren, and H. Xu. 2012. TPC proteins are phosphoinositide- activated sodium-selective ion channels in endosomes and lysosomes. *Cell*. 151:372–383. doi:10.1016/j.cell.2012.08.036.

Waterman-Storer, C.M., and E.D. Salmon. 1998. Endoplasmic reticulum membrane tubules are distributed by microtubules in living cells using three distinct mechanisms. *Current Biology*. 8:798–807. doi:10.1016/S0960-9822(98)70321-5.

Westrate, L.M., J.E. Lee, W.A. Prinz, and G.K. Voeltz. 2015. Form follows function: the importance of endoplasmic reticulum shape. *Annu Rev Biochem*. 84:791–811. doi:10.1146/annurev-biochem-072711-163501.

Wu, H., and G.K. Voeltz. 2021. Reticulon-3 Promotes Endosome Maturation at ER Membrane Contact Sites. *Developmental Cell*. 56:52-66.e7. doi:10.1016/j.devcel.2020.12.014.

Zolov, S.N., D. Bridges, Y. Zhang, W.-W. Lee, E. Riehle, R. Verma, G.M. Lenk, K. Converso-Baran, T. Weide, R.L. Albin, A.R. Saltiel, M.H. Meisler, M.W. Russell, and L.S. Weisman. 2012. In vivo, Pikfyve generates PI(3,5)P2, which serves as both a signaling lipid and the major precursor for PI5P. *Proceedings of the National Academy of Sciences of the United States of America*. 109:17472–7. doi:10.1073/pnas.1203106109.

Data availability statement

All data and original tools built in this study will be available upon request.

Funding and conflict of interest statement

RJB was a recipient of a Canada Research Chair (#950-232333) with contributions from Toronto Metropolitan University and Faculty of Science. The Natural Sciences and Engineering Research Council (NSERC) of Canada funded this research with Discovery research grant to RJB (RGPIN-2020-04343). NRA was partly funded by an NSERC Undergraduate Student Research

Award. Canada Foundation for Innovation with contributions from the Ministry of Training, Colleges, and Universities of Ontario and from Toronto Metropolitan supported this work with John Evans Leadership Fund to RJB (#32957 and #38151). The authors have no conflict to declare.

Acknowledgements

We would like to thank Dr. Camilla Raiborg (Oslo University Hospital) for kindly providing the plasmids encoding the GFP fusion of the wild-type and of the FYVE4A mutant of protrudin. We also thank Kimberly Lau at the Sick Kids Imaging Facility for advice on Imaris and 3D reconstruction.

Figure Legends

Figure 1: Overexpression of ER morphogenic proteins does not mimic PIKfyve inhibition in COS-7 cells. (A, B) Confocal images of COS-7 cells labeled with fluorescent dextran (magenta) and transiently expressing mCherry-CLIMP63 or mCherry (gray; A), or eGFP-Rtn4a or eGFP (gray; B). Cells were exposed to either 0.01% DMSO (vehicle) or 80 nM apilimod for 2 h. Scale

1142 bar = 20 µm. **(C-D)** Quantification of lysosome number (C) and volume (D) upon expression of
1143 CLIMP63 to induce ER sheets. **(E-F)** Quantification of lysosome number (E) and volume (F) upon
1144 expression of Rtn4a to promote ER tubulation. All experiments were repeated four
1145 independent times. Data points from matching independent experiments are colour coded.
1146 Shown are the mean ± SEM. Data are based on 30-50 transfected cells per condition per
1147 experiment and analyzed using repeated measures two-way ANOVA and Tukey's multiple
1148 comparisons test; p values are shown.
1149
1150 **Figure 2: PIKfyve loss of function alters the ER architecture. (A)** Confocal images of COS-7 cells
1151 transiently transfected with ER-mNeonGreen (gray), labeled with fluorescent Dextran
1152 (magenta), and treated with 0.01% DMSO (vehicle) or 80 apilimod for 2 h. **(B)** Image analysis
1153 strategy to quantify ER morphometrics whereby a fluorescence image is converted to an ER
1154 mask, skeletonized, and analysed for skeletal length, branch number, and junction number. **(C)**
1155 ER-mNeonGreen and corresponding skeletonized images of a cell treated with vehicle or
1156 apilimod. Scale bar: full size = 20 µm, zoom insert = 5 µm. **(D-G)** Quantification of ER
1157 morphology including ER skeletal length (D), number of ER junctions per cell (E), number of
1158 branches per cell (F), and average branch length (µm) (G). All experiments were repeated four
1159 independent times. Data points from matching independent experiments are colour coded.
1160 Shown are the mean ± SEM. Data are based on 15-20 transfected cells per condition per
1161 experiment. Data was analysed using a two-tailed paired Student's t-test and p values are
1162 shown.
1163

1164 **Figure 3: ER motility is reduced in PIKfyve inhibited cells. (A)** Strategy to quantify ER motility
1165 from timelapse images, optic flow analysis and membrane displacement by grouping pixel
1166 changes per frame as indicated. **(B)** Representative time-lapse confocal images of COS-7 cells
1167 transiently transfected with ER-mNeonGreen (gray). Zoom inserts show ER redistribution as
1168 indicated by the white arrow. Cells were exposed to either 0.02% DMSO (vehicle) or 240 nM
1169 apilimod for 2 h. **(C-E)** Quantification of membrane displacement analysis categorized by low
1170 movement (C), intermediate movement (D), and rapid movement (E). **(F)** Confocal images of
1171 COS-7 cells transiently transfected with ER-mNeonGreen (gray), labeled with fluorescent
1172 dextran (magenta), and exposed to either 0.02% DMSO (vehicle) or 240 nM apilimod. Zoom
1173 inserts show an ER-hitchhiking event occurring over 2.5 seconds as indicated by the white
1174 arrow. Scale bar: full size = 20 µm, zoom insert = 5 µm. **(G)** Quantification of the number of ER-
1175 hitchhiking events that occurred in a 100 μm^2 ROI over one minute, repeated three
1176 independent times. Data from *C-E* are from five independent experiments and based on 7
1177 randomized ROIs from 7-10 transfected cells, per condition per experiment. Data in G are from
1178 three experiments and based on 5 randomized ROIs from 15-20 transfected cells, per condition
1179 per experiment. Data points from matched experiments are colour-coded. Shown is the mean
1180 $\pm$ SEM, analysed using a two-tailed paired Student's t-test; p values are shown.
1181

1182 **Figure 4. PIKfyve activity supports lysosome motility and spatial distribution. (A)** Confocal
1183 images of COS-7 cells labeled with Alexa Fluor 647-Dextran (magenta) and exposed to either
1184 0.02% DMSO (vehicle) or 240 nM apilimod for 2 h. Scale bar = 20 µm. **(B)** Schematic
1185 representation of the changes to lysosome spatial distribution between control and PIKfyve

1186 inhibited conditions. **(C)** Quantification of the distribution of lysosomes in the perinuclear
1187 region versus the peripheral region of the cell. A ratio of the number of lysosomes in the
1188 perinuclear region to total number of lysosomes in the cell was determined – the same was
1189 done for the peripheral region respectively. **(D-F)** Quantification of lysosome motility including
1190 track mean speed (D), total distance travelled (E), and track displacement (F). (**G)** Kymograph of
1191 lysosome movement along a linear ROI. The vertical axis represents time (s), and the horizontal
1192 axis represents distance along a selected path. Diagonal or segmented lines indicate motility;
1193 vertical lines represent stationary organelles. All experiments were repeated four independent
1194 times. Data points from matching independent experiments are colour coded. Shown is the
1195 mean $\pm$ SEM. Data were analysed using a two-way ANOVA and Tukey's multiple comparison
1196 test for (C) and two-tailed paired Student's t-test for (D-F); p values are shown.
1197
1198 **Figure 5. Loss of PIKfyve activity likely alters the molecular configuration of ER-lysosome**
1199 **contact sites. (A-C)** Confocal images of HeLa cells treated with 0.02% DMSO (vehicle), 240 nM
1200 apilimod, or 1 µM YM-201636 for 2 h followed by Proximity Ligation Assay between protrudin
1201 and VapA (A), or Rab7 and VAPA (B), or Rab7 and protrudin (C). Scale bar = 15 µm. **(G-K)**
1202 Confocal images of HeLa cells treated with 0.02% DMSO (vehicle) or 240 nM apilimod for 2 h
1203 followed by Proximity Ligation Assay between FYCO1 and VAPA (G), or protrudin (H), or Rab7
1204 (I), or kinesin-1 (J), and between Rab7 and kinesin-1 (K). Images were generated by maximum
1205 projection of z-stacks of the PLA signal (magenta); DAPI-stained nucleus is shown in gray.
1206 Negative controls where one of the primary antibodies was missing are shown in Sup. Fig.5A-H.
1207 Scale bar = 15 µm. **(D-F, L-P)** Quantification of the number of PLA dots per cell for each protein

1208 pair tested in A-C and G-K, as indicated. Experiments in D-F and K were repeated four
1209 independent times, while those in G-K were done three times. Data points were colour coded
1210 to match to respective experiment. Shown is the mean ± SEM. Data were analysed using an
1211 Ordinary one-way ANOVA and Dunnett's multiple comparisons test (D-F) and paired Student's
1212 t-test (L-P); p values are shown.
1213
1214 **Figure 6. Protrudin and PtdIns(3)P are required for ER remodelling during PIKfyve inhibition.**
1215 **(A)** Confocal images of U2OS cells co-transfected with non-targeting siRNA control or siRNA
1216 oligonucleotides against protrudin, and ER-mScarletI (gray), or **(B)** labeled with fluorescent
1217 dextran (magenta). **(C-F)** Quantitative analysis of ER and lysosomal morphology based on ER-
1218 mScarletI or dextran fluorescence in conditions shown (A): number of ER branches per cell (C),
1219 number of ER junctions per cell (D), average number of lysosome per cell (E), and average
1220 lysosome volume (F). **(G)** Confocal images of COS-7 cells transfected with ER-mNeonGreen
1221 (gray), labelled with fluorescent dextran (magenta), and then exposed to either 0.02% DMSO
1222 (vehicle), 240 nM apilimod, 1 µM VPS34-In1, or apilimod and VPS34-In1 for 2 h. Scale bar: full
1223 size = 20 µm **(H-K)** Quantification of ER morphology including number of ER branches per cell
1224 (H), number of ER junctions per cell (I), and quantification of average lysosome number per cell
1225 (J), and average lysosome volume (K). All experiments were repeated three independent times.
1226 Data points from matching independent experiments are colour coded. Shown are the mean ±
1227 SEM. Data were based on 20-25 transfected cells per condition per experiment. Data in (C-F)
1228 was analyzed using a two-way ANOVA and Tukey's multiple comparisons test, and data in (H-K)
1229 was analyzed using a one-way ANOVA and Dunnett's post-hoc test; p values are shown.

1230

1231 **Figure 7. Protrudin hyper-tethers ER and lysosomes during PIKfyve inhibition to alter ER**
1232 **morphology. (A)** Confocal images of HeLa cells co-transfected with non-targeting siRNA control
1233 or siRNA oligonucleotides against protrudin, and protrudin^{wt}-GFP or protrudin^{FYVE4A}-GFP (gray).
1234 Cells were labeled with fluorescent dextran (magenta) and then exposed to either 0.02% DMSO
1235 (vehicle) or 240 nM apilimod for 2 h. Scale bar: full size = 20 µm, zoom insert = 5 µm. **(B, C)**
1236 Number of protrudin branches per cell (B) and junctions per cell (C) based on protrudin^{wt}-GFP
1237 or protrudin^{FYVE4A}-GFP fluorescence. **(D,E)** Confocal images of COS7 cells transfected with
1238 2FYVE-RFP (D; grayscale) or protrudin^{wt}-GFP (E; grayscale), labelled with fluorescent dextran
1239 (magenta), and then exposed to either 0.02% DMSO (vehicle), 240 nM apilimod, 1 µM VPS34-
1240 In1, or apilimod and VPS34-In1 for 2 h. Scale bar: full size = 20 µm. **(F, G)** Quantification of ER
1241 morphology by number of ER branches per cell (F) and number of ER junctions per cell (G) in
1242 cells shown in E. **(H, I)** Quantification of lysosome number per cell (H) and lysosome volume (I)
1243 in cells shown in E. All experiments were repeated three independent times. Data points from
1244 matching independent experiments are colour coded. Shown are the mean $\pm$ SEM. Data are
1245 based on 20-25 transfected cells per condition per experiment. Data from (B-C) was analyzed
1246 using a three-way ANOVA and Tukey's multiple comparisons test, and data from (F-I) was
1247 analysed using a one-way ANOVA and Dunnett's post-hoc test; p values are shown.

1248

1249 **Figure 8. Protrudin and its FYVE domain are required for ER-lysosome changes induced by**
1250 **PIKfyve inactivation (A-B)** Confocal images of HeLa cells transfected with non-targeting siRNA
1251 control or siRNA oligonucleotides against protrudin and treated with 0.02% DMSO (vehicle) or

1252 240 nM apilimod for 2 h followed by Proximity Ligation Assay between protrudin and Rab7 (A),
1253 or Rab7 and VAPA (B). Scale bar: full size = 20 µm. **(C-D)** Quantification of number of PLA dots
1254 between protrudin and Rab7 (C) and Rab7 and VAPA (D) in control silenced and protrudin-
1255 silenced cells with and without apilimod. **(E)** Quantification of PLA dots between Rab7 and
1256 protrudin in mock-silenced (siNT) or protrudin-silenced cells expressing protrudin^{wt}-GFP or
1257 protrudin^{FYVE4A}-GFP exposed to either vehicle or apilimod. All experiments were repeated three
1258 independent times and colour-code matched. Shown is the mean $\pm$ SEM. Data for (C-D) were
1259 analyzed using a two-way ANOVA and Tukey's multiple comparison test, and data for (E) was
1260 analyzed using a three-way ANOVA and Tukey's multiple comparisons test; p-values are shown.
1261
1262 **Figure 9. ER-lysosome hyper-tethering with inducible dimerization system suffices to distort**
1263 **the ER architecture. (A)** Confocal images of COS-7 cells transiently transfected with iRFP-FRB-
1264 Rab7 (magenta) and FKBP-mCherry-protrudin^{wt} or FKBP-mCherry-protrudin^{FYVE4A} (gray). Cells
1265 were exposed to either no treatment, 100 nM rapamycin for 15 min, VPS34-In1 for 2 h, or
1266 VPS34-In1 and rapamycin combined. Scale bar: full size = 20 µm. **(B-D)** Quantification of
1267 protrudin-based ER morphology including skeletal length (B), number of branches per cells (C),
1268 and number of junctions per cell (D) in the indicated conditions. Experiments (B-D) were
1269 repeated three independent times and colour-code matched. Shown is the mean $\pm$ SEM. Data
1270 for (F-H) were analyzed using a two-way ANOVA and Tukey's multiple comparisons test; p-
1271 values shown.
1272
1273

1274 **Supplementary Figure Legend**

1275 **Supplementary Figure S1. ER morphology and dynamics are altered upon PIKfyve inhibition**
1276 **using YM-201636. (A)** Confocal images of COS-7 cells transiently transfected with ER-
1277 mNeonGreen (gray) and labelled with Dextran, Alexa-647 (magenta). Cells were exposed to
1278 either 0.02% DMSO (vehicle) or 1 µM YM-201636 for 2 h. **(B-E)** Quantification of ER morphology
1279 including ER skeletal length (B), number of ER junctions per cell (C), number of branches per cell
1280 (D), and average branch length (E). **(F)** Representative time-lapse confocal images of COS-7 cells
1281 transiently transfected with ER-mNeonGreen (gray). Skeletonize function can be applied to
1282 trace ER morphology. Zoom inserts show ER redistribution over 40 s; white arrowheads
1283 exemplify morphological changes. Scale bar: full size = 20 µm, zoom insert = 5 µm. **(G-I)**
1284 Quantification of membrane displacement analysis categorized by low movement (G),
1285 intermediate movement (H), and rapid movement (I). Experiments (B-E) were repeated four
1286 independent times; Experiments (G-I) were repeated six independent times. Data points from
1287 matching independent experiments are colour coded. Shown in the mean $\pm$ SEM. Data from B
1288 through E are based on 15-20 transfected cells per condition per experiment. Data from G
1289 through I are based on 7 randomized ROIs for 7-10 transfected cells, per condition per
1290 experiment. Data were analyzed using a two-tailed Student's t-test and p values are shown.

1291

1292 **Supplementary Figure S2. Voids in ER architecture are filled with vacuolated endosomes and**
1293 **lysosomes upon PIKfyve inhibition. (A-B)** Confocal images of COS-7 cells labeled with Dextran,
1294 Alexa Fluor 647 (magenta) and transiently expressing ER-mNeonGreen (gray) or mCherry (cyan)
1295 (A) or mRFP-Rab5 (cyan) (B). Cells were exposed to either 0.01% DMSO or 80 nM apilimod for 2

1296 h. Scale bar: full size = 20 µm, zoom insert = 5 µm. **(C-D)** Quantification of Mander's Analysis
1297 done on the colocalization between Dextra, Alexa 647 and mRFP-Rab5. All experiments were
1298 repeated three independent times. Data points from matching independent experiments are
1299 colour coded and shown as mean ± SEM from 30-50 transfected cells per condition per
1300 experiment. Data were analyzed using a two-tailed Students t-test and p values are shown.
1301
1302 **Supplementary Figure S3. Vac14 silencing disturbs ER morphology. (A)** Representative
1303 Western blot of Vac14 from U2OS cells transfected with non-targeting siRNA control (siNT) or
1304 one of two siRNA oligonucleotides against Vac14. GAPDH was used as a loading control. **(B)**
1305 Quantitative analysis displaying Vac14 protein levels normalized to GADPH after Vac14
1306 silencing. **(C)** Confocal images of U2OS cells co-transfected with either non-targeting siRNA or
1307 siRNA oligonucleotides against Vac14 and ER-mScarletI (gray) followed by an
1308 immunofluorescence staining to LAMP1 (magenta). Scale bar: full size = 20 µm, zoom insert = 5
1309 µm. **(D-G)** Quantitative analysis of ER morphology in control or Vac14-silenced cells using
1310 skeletal length (D), number of branches per cell (E), number of junctions per cell (F), and
1311 average branch length (G). All experiments were repeated three independent times. Data
1312 points from matching independent experiments are colour coded and shown as mean ± STD (B)
1313 and mean ± SEM (D-G). Data from (D-G) were obtained from 20-25 transfected cells per
1314 condition per experiment. Data were analyzed using a one-way ANOVA and Dunnett's multiple
1315 comparisons test.
1316

1317 **Supplemental Figure S4. PIKfyve inhibition does not significantly affect microtubule**
1318 **architecture and dynamics. (A)** Confocal images of HeLa cells immunostained for α-tubulin
1319 (gray) and LAMP1 (magenta) treated with 0.02% DMSO (vehicle), 240 nM apilimod or 1 µM YM-
1320 201636 for 2 h. Scale bar = 20 µm **(B-D)** Quantification of microtubule morphology including
1321 number of branches per cell (B), number of junctions per cell (C), and average branch length
1322 (D). For B through D, all experiments were repeated four independent times. **(E)** Confocal
1323 images of COS-7 cells transiently transfected with EB1-GFP displayed as Rainbow RBG LUT and
1324 treated as in A. Scale bar: full size = 20 µm, zoom insert = 5 µm. **(F-H)** Semi-quantification of
1325 microtubule dynamics including percentage of cells with >10 EB1-puncta (F), percentage of cells
1326 with mobile EB1-puncta (G), and percentage of cells with EB1-puncta moving away from the
1327 nucleus (H). For F-H, all experiments were repeated three independent times. For B-D and F-H,
1328 data was analyzed using an Ordinary one-way ANOVA test and Dunnett's multiple comparisons
1329 test.
1330
1331 **Supplementary Figure 5. Rab7 GTPase status appears unaltered in PIKfyve-inhibited cells. (A-**
1332 **H)** Control confocal images of HeLa cells treated with one individual primary antibody only for
1333 each PLA test for protrudin and VAPA (A), Rab7 and VAPA (B), Rab7 and protrudin (C), FYCO1
1334 and VAPA (D), FYCO1 and protrudin (E), FYCO1 and Rab7 (F), Rab7 and kinesin-1 (G) and FYCO1
1335 and kinesin-1 (H). Scale bar= 15 µm. **(I)** HeLa cells immuno-stained for LAMP1 (magenta) and
1336 Rab7 (gray) following treatment with 0.02% DMSO (vehicle) and 240 nM apilimod for 2 h. Scale
1337 bar= 20 µm. **(J-K)** Quantitative analysis displaying the average Mander's Coefficient for the
1338 fraction of Rab7 colocalized with LAMP1 (J), and fraction of LAMP1 colocalized with Rab7 (K). **(L)**

1339 Representative Western blots of affinity purification of Rab7-GTP using GST-RILPC33, displaying
1340 total Rab7 levels from input samples and GTP-Rab7 levels recovered with the GST negative
1341 control and GST-RILPC33 from cells exposed to 0.02% vehicle (DMSO), 240 nM apilimod or 1
1342 µM YM-201636 for 2 h. **(M)** Quantitative analysis of affinity precipitated GTP-Rab7 from GST
1343 negative control and GST-RILPC33. GST-control and GST-RILPC33 were normalized first to input
1344 levels of β-actin and then Rab7. All experiments were repeated three independent times. Data
1345 points from matching independent experiments are colour coded. Data shown in J through K
1346 are shown as the mean ± SEM and analyzed using a two-tailed Student's t-test. Data from M is
1347 shown as the mean ± STD and was analyzed using a two-way ANOVA and Tukey's multiple
1348 comparisons test; p values are shown.
1349
1350
1351 **Supplementary Figure 6. Three-dimensional reconstruction of protrudin-positive ER. (A)**
1352 Representative Western blots of non-targeting siRNA control or siRNA oligonucleotides against
1353 protrudin displaying protrudin and clathrin levels. **(B)** Quantitative analysis displaying protrudin
1354 protein levels upon transfection with siNT or siProtrudin after normalized to loading control,
1355 clathrin. **(C)** Three-dimensional reconstruction of HeLa cells co-transfected with non-targeting
1356 siRNA control or siRNA oligonucleotides against protrudin, and expressing protrudin^{wt}-GFP or
1357 protrudin^{FYVE4A}-GFP (gray). Cells were labeled with Dextran, Alexa 546 (magenta) and then
1358 exposed to either 0.02% DMSO (vehicle) or 240 nM apilimod for 2 h. Scale bar: full frame = 20
1359 µm, zoom insert = 0.7 µm. All experiments were repeated three independent times. Data points

1360 from matching independent experiments are colour coded. Shown in the mean ± STD. Data
1361 was analyzed using a two-tailed Student's t-test and p values are shown.
1362
1363 **Supplementary Figure 7. PIKfyve inhibition leads to global ER changes across different**
1364 **resident proteins. (A-F)** Quantitative analysis of COS7 cells transfected with mCherry-CLIMP63
1365 (A-C, as shown in Fig. 1A) or GFP-Rtn4a (D-F, as in Fig. 1B) upon treatment with either 0.02%
1366 DMSO (vehicle) or 80 nM apilimod for 2 h. ER morphometrics were analyzed including skeletal
1367 length (A, D), number of branches per cell (B, E) and number of junctions per cell (C, F). **(G)**
1368 Confocal images of COS7 cells co-transfected with GFP-Atlastin1 and GFP-protrudin^{wt}, followed
1369 by treatment with either 0.02% DMSO (vehicle) or 80 nM apilimod for 2 h. Scale bar = 20 µm.
1370 **(H-I)** Quantitative analysis of ER morphometrics using Atlastin-1 fluorescence using number of
1371 branches per cell (H) and number of junctions per cell (I). Experiments from (A-F) were
1372 repeated four independent times; experiments from (H-I) were repeated three independent
1373 times. Data points from matching independent experiments are colour coded. Shown is the
1374 mean ± SEM. Data was analyzed using a two-tailed Student's t-test and p values are shown.
1375
1376 **Supplementary Video Legend**
1377 **Supplemental Video 1. ER motility is retained upon treatment with vehicle control (DMSO).**
1378 COS-7 cells were transiently transfected with ER-mNeonGreen (gray) and treated with 0.02%
1379 vehicle (DMSO) for 2 h. The ER network undergoes continuous remodeling through tubule
1380 extension, retraction, and branching, reflecting its highly dynamic and interconnected nature.

1381 Time-lapse images were acquired at a rate of 4 frame/s for 1 minute. Still frames from Video 1
1382 are displayed in Figure 3A. Scale bar: 20 µm.
1383
1384 **Supplemental Video 2. ER motility is reduced upon acute treatment with PIKfyve inhibitor**
1385 **Apilimod.** COS-7 cells were transiently transfected with ER-mNeonGreen (gray) and treated
1386 with 240 nM apilimod for 2 h. Time-lapse images were acquired at a rate of 4 frame/s for 1
1387 minute. Still frames from Video 2 are displayed in Figure 3A. Scale bar: 20 µm.
1388
1389 **Supplemental Video 3. ER motility is reduced upon acute treatment with PIKfyve inhibitor**
1390 **YM-201636.** COS-7 cells were transiently transfected with ER-mNeonGreen (gray) and treated
1391 with 1 µM YM-201636 for 2 h. Time-lapse images were acquired at a rate of 4 frame/s for 1
1392 minute. Still frames from Video 3 are displayed in Supplemental Figure 2A. Scale bar: 20 µm.
1393
1394 **Supplemental Video 4. EB1-GFP dynamics under vehicle condition conditions.** COS-7 cells
1395 were transiently transfected with EB1-GFP displayed as a rainbow LUT scale, where red is the
1396 highest intensity level and blue is the lowest intensity level. Cells were treated with 0.02%
1397 vehicle (DMSO) for 2 h. EB1-GFP comets mark the plus-ends of growing microtubules, enabling
1398 visualization of dynamic microtubules. Time-lapse images were acquired at a rate of 4 frame/s
1399 for 1 minute. Still frames from Video 4 are displayed in Figure 4E. Scale bar: 20 µm.
1400
1401 **Supplemental Video 5. EB1-GFP dynamics appear unaltered upon PIKfyve inhibition using**
1402 **apilimod.** COS-7 cells were transiently transfected with EB1-GFP displayed as a rainbow LUT

1403 scale, where red is the highest intensity level and blue is the lowest intensity level. Time-lapse
1404 images were acquired at a rate of 4 frame/s for 1 minute. Still frames from Video 5 are
1405 displayed in Figure 4E. Scale bar: 20 µm.
1406
1407 **Supplemental Video 6. Microtubule EB1 dynamics remain unaffected by YM-201636**
1408 **treatment.** COS-7 cells were transiently transfected with EB1-GFP displayed as a rainbow LUT
1409 scale, where red is the highest intensity level and blue is the lowest intensity level. Time-lapse
1410 images were acquired at a rate of 4 frame/s for 1 minute. Still frames from Video 6 are
1411 displayed in Figure 4E. Scale bar: 20 µm.
1412
1413 **Supplemental Video 7. Normal ER-movement via organelle hitchhiking in vehicle-treated**
1414 **cells.** COS-7 cells were transiently transfected with ER-mNeonGreen (gray) and labeled with
1415 Dextran, Alexa 647 (magenta) followed by treatment with 0.02% vehicle (DMSO) for 2 h.
1416 Positive hitchhiking events were scored based on ER movement driven by physical association
1417 with a motile dextran labelled lysosome. Timelapse images were acquired at a rate of 3.3
1418 frames/s for 1 minute. Still frames from Video 7 are displayed in Figure 4J. Scale bar: 20 µm.
1419
1420 **Supplemental Video 8. ER-hitchhiking frequency drops upon PIKfyve inhibition.** COS-7 cells
1421 were transiently transfected with ER-mNeonGreen (gray) and labeled with Dextran, Alexa 647
1422 (magenta) followed by treatment with 240 nM apilimod for 2 h. Positive hitchhiking events
1423 were scored based on ER movement driven by physical association with a motile dextran

1424 labelled lysosome. Timelapse images were acquired at a rate of 3.3 frames/s for 1 minute. Still

1425 frames from Video 7 are displayed in Figure 4J. Scale bar: 20 µm.

1426

FIGURE 1.

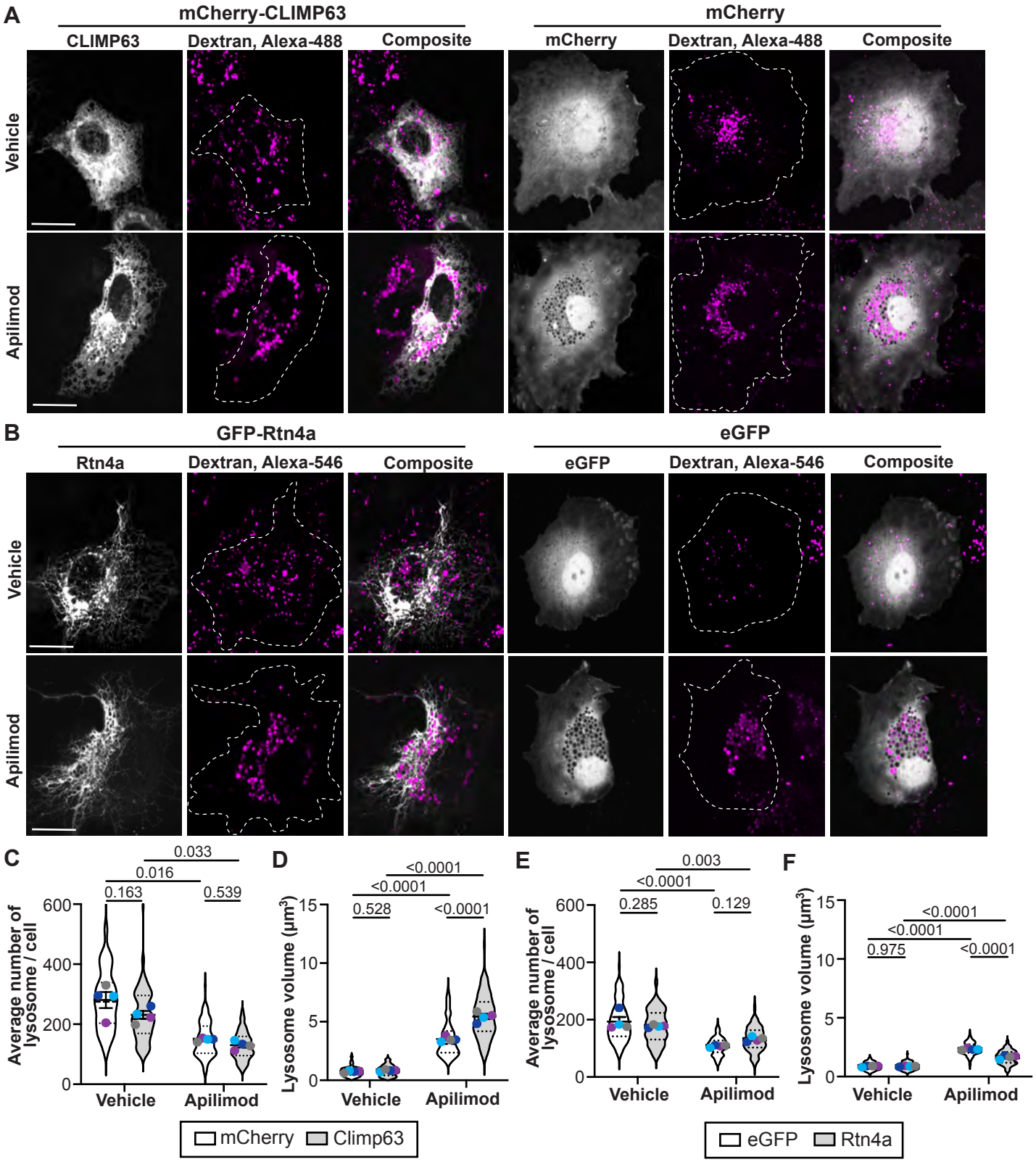
A
mCherry-CLIMP63
mCherry
CLIMP63
Dextran, Alexa-488
Composite
mCherry
Dextran, Alexa-488
Composite
Vehicle
Apilimod
B
GFP-Rtn4a
eGFP
Rtn4a
Dextran, Alexa-546
Composite
eGFP
Dextran, Alexa-546
Composite
Vehicle
Apilimod
C
Average number of lysosome / cell
0.033
0.016
0.163
0.539
Vehicle
Apilimod
D
Lysosome volume (µm³)
<0.0001
<0.0001
0.528
<0.0001
Vehicle
Apilimod
E
Average number of lysosome / cell
0.003
<0.0001
0.285
0.129
Vehicle
Apilimod
F
Lysosome volume (µm³)
<0.0001
<0.0001
0.975
<0.0001
Vehicle
Apilimod
mCherry
Climp63
eGFP
Rtn4a

FIGURE 2.

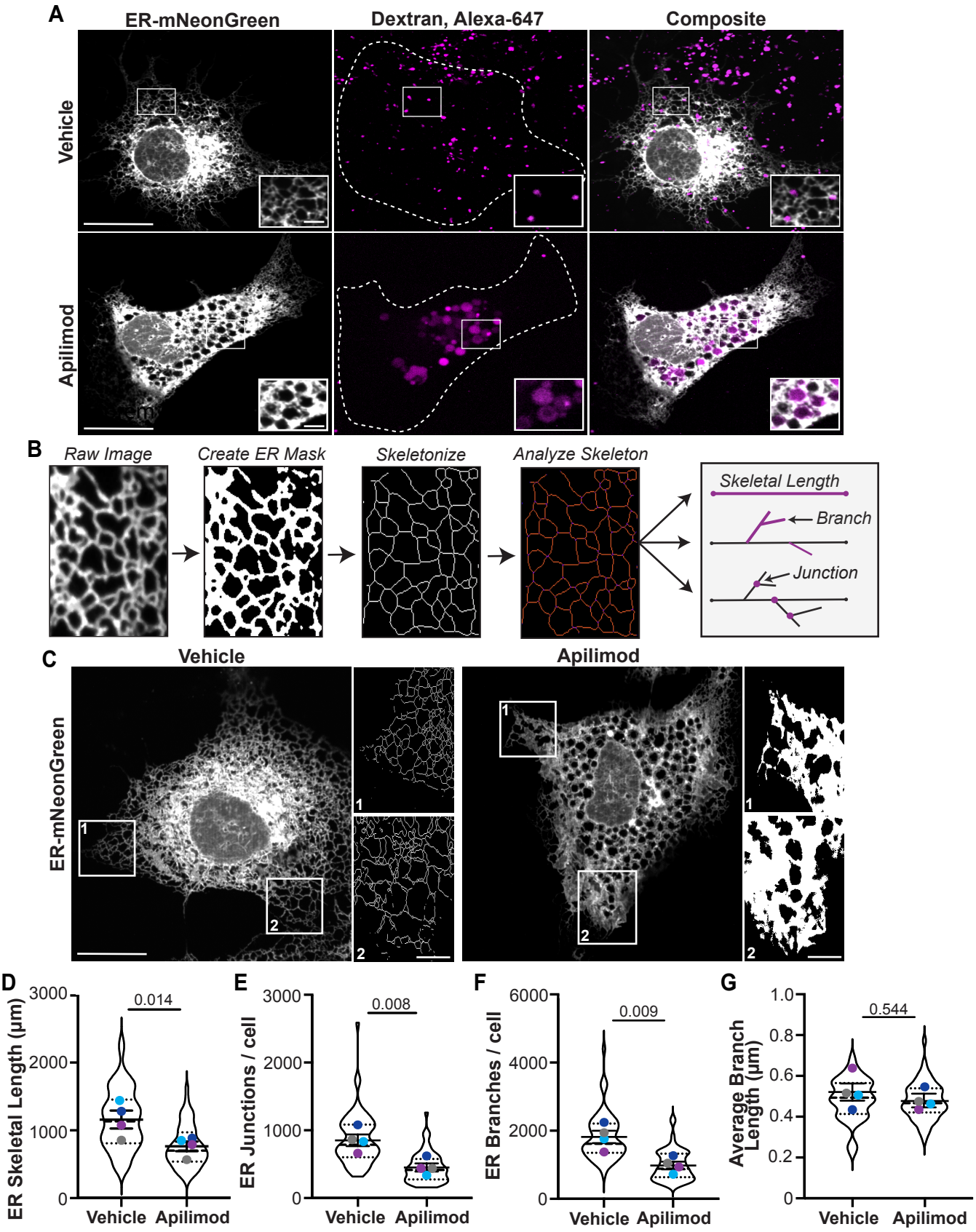
A
ER-mNeonGreen
Dextran, Alexa-647
Composite
Vehicle
Apilimod
B
Raw Image
Create ER Mask
Skeletonize
Analyze Skeleton
Skeletal Length
Branch
Junction
C
Vehicle
Apilimod
ER-mNeonGreen
D
ER Skeletal Length (µm)
0.014
E
ER Junctions / cell
0.008
F
ER Branches / cell
0.009
G
Average Branch Length (µm)
0.544
Vehicle
Apilimod

FIGURE 3.

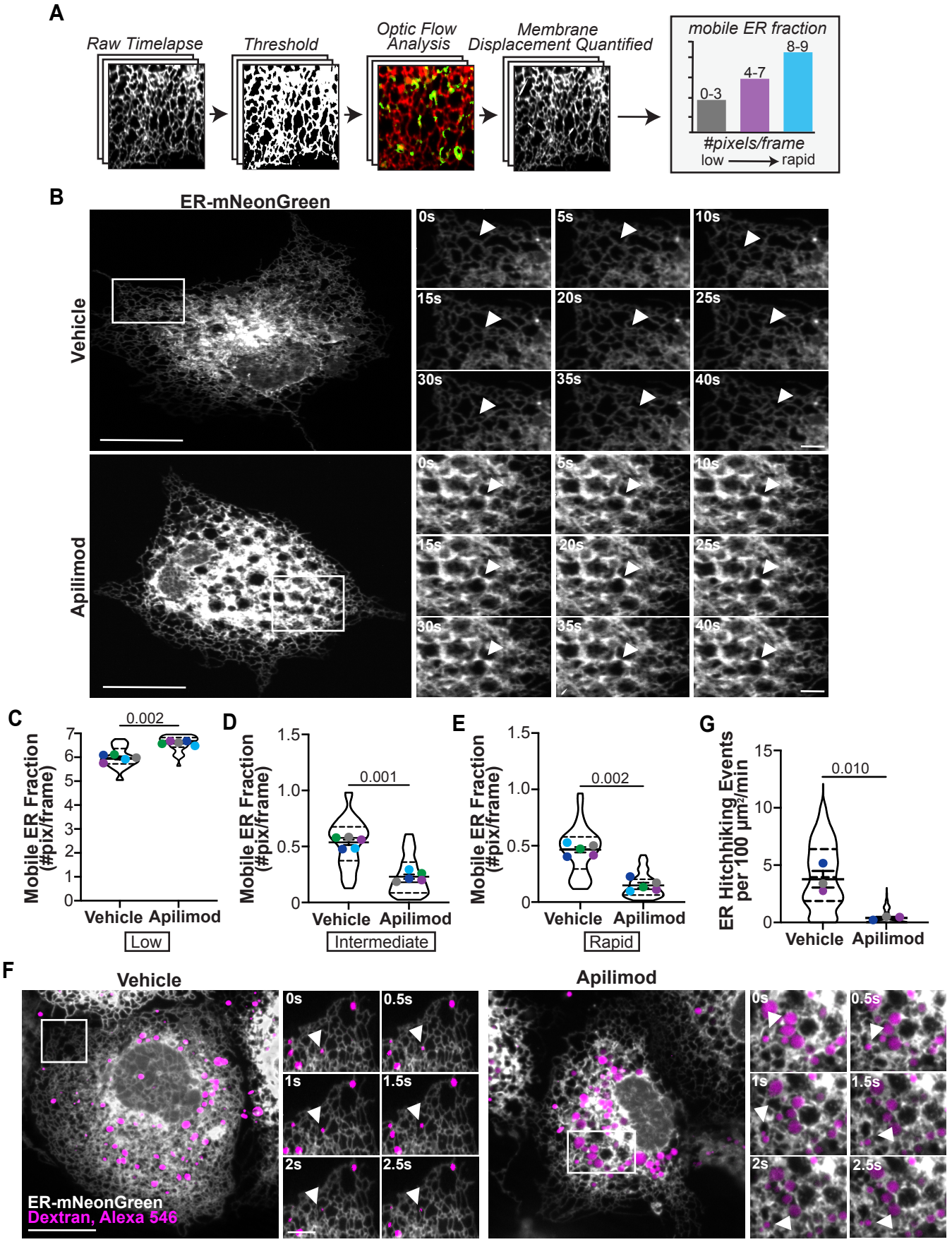
A
Raw Timelapse
Threshold
Optic Flow Analysis
Membrane Displacement Quantified
mobile ER fraction
0-3
4-7
8-9
#pixels/frame
low
rapid
B
ER-mNeonGreen
Vehicle
Apilimod
0s
5s
10s
15s
20s
25s
30s
35s
40s
C
Mobile ER Fraction (#pix/frame)
0.002
Vehicle
Apilimod
Low
D
Mobile ER Fraction (#pix/frame)
0.001
Vehicle
Apilimod
Intermediate
E
Mobile ER Fraction (#pix/frame)
0.002
Vehicle
Apilimod
Rapid
G
ER Hitchhiking Events per 100 µm²/min
0.010
Vehicle
Apilimod
F
Vehicle
Apilimod
0s
0.5s
1s
1.5s
2s
2.5s
ER-mNeonGreen
Dextran, Alexa 546

FIGURE 4.

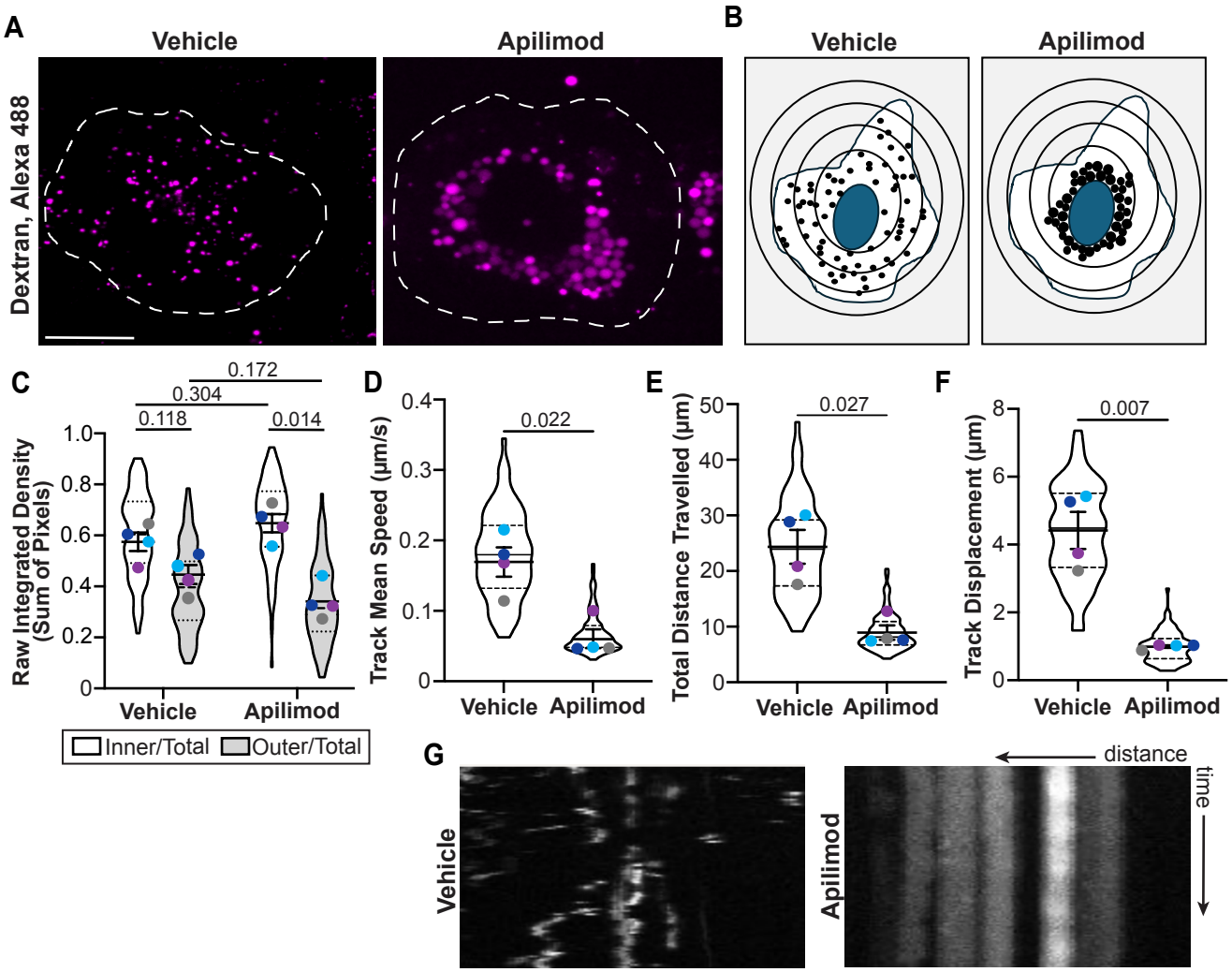
A
Vehicle
Apilimod
Dextran, Alexa 488
B
Vehicle
Apilimod
C
0.172
0.304
0.118
0.014
Raw Integrated Density (Sum of Pixels)
1.0
0.8
0.6
0.4
0.2
0
Vehicle
Apilimod
Inner/Total
Outer/Total
D
0.022
Track Mean Speed (µm/s)
0.4
0.3
0.2
0.1
0
Vehicle
Apilimod
E
0.027
Total Distance Travelled (µm)
50
40
30
20
10
0
Vehicle
Apilimod
F
0.007
Track Displacement (µm)
8
6
4
2
0
Vehicle
Apilimod
G
Vehicle
Apilimod
distance
time

FIGURE 5.

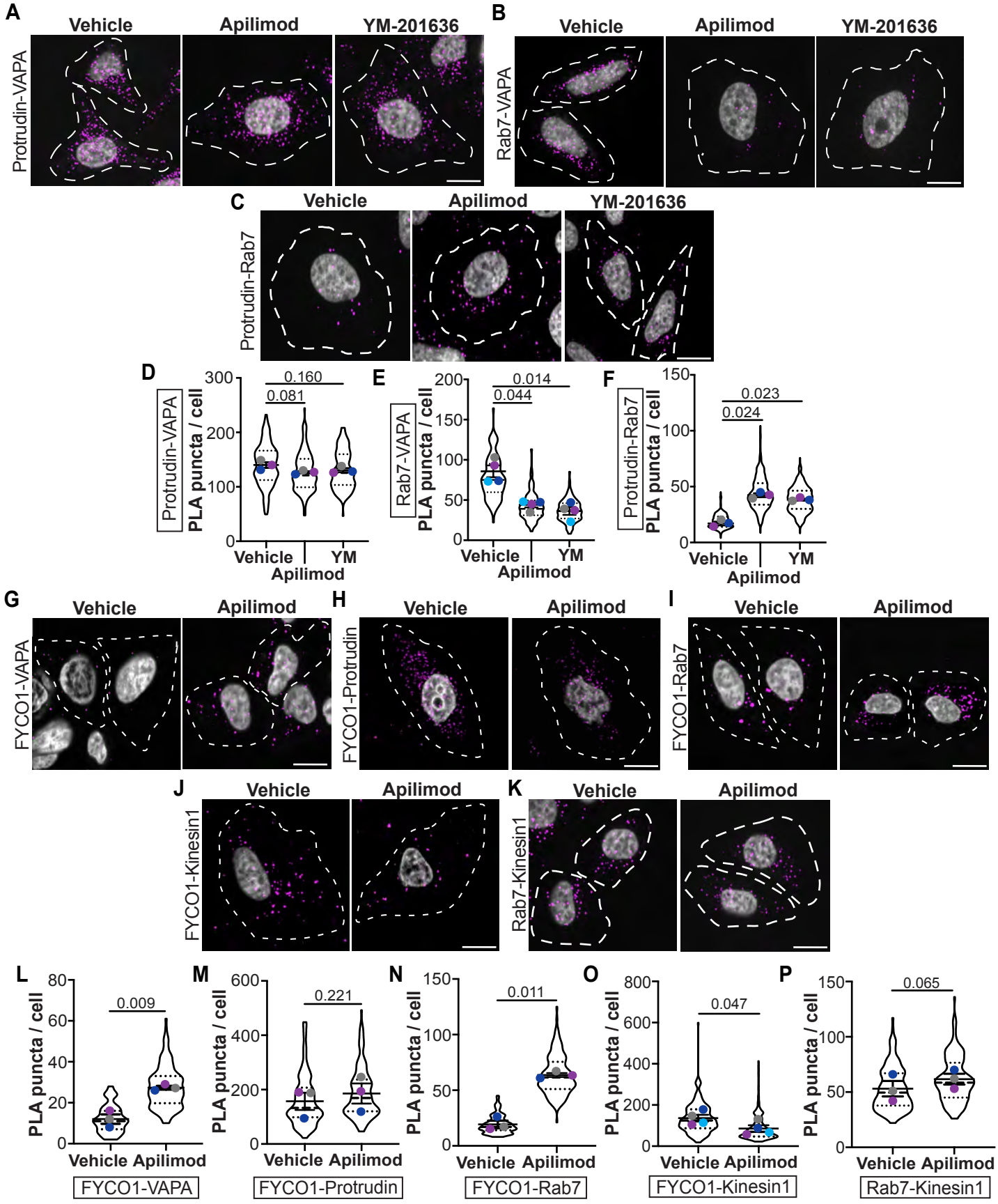
A
Vehicle
Apilimod
YM-201636
Protrudin-VAPA
B
Vehicle
Apilimod
YM-201636
Rab7-VAPA
C
Vehicle
Apilimod
YM-201636
Protrudin-Rab7
D
Protrudin-VAPA
PLA puncta / cell
0.160
0.081
Vehicle
YM
Apilimod
E
Rab7-VAPA
PLA puncta / cell
0.014
0.044
Vehicle
YM
Apilimod
F
Protrudin-Rab7
PLA puncta / cell
0.023
0.024
Vehicle
YM
Apilimod
G
Vehicle
Apilimod
FYCO1-VAPA
H
Vehicle
Apilimod
FYCO1-Protrudin
I
Vehicle
Apilimod
FYCO1-Rab7
J
Vehicle
Apilimod
FYCO1-Kinesin1
K
Vehicle
Apilimod
Rab7-Kinesin1
L
PLA puncta / cell
0.009
Vehicle Apilimod
FYCO1-VAPA
M
PLA puncta / cell
0.221
Vehicle Apilimod
FYCO1-Protrudin
N
PLA puncta / cell
0.011
Vehicle Apilimod
FYCO1-Rab7
O
PLA puncta / cell
0.047
Vehicle Apilimod
FYCO1-Kinesin1
P
PLA puncta / cell
0.065
Vehicle Apilimod
Rab7-Kinesin1

FIGURE 6.

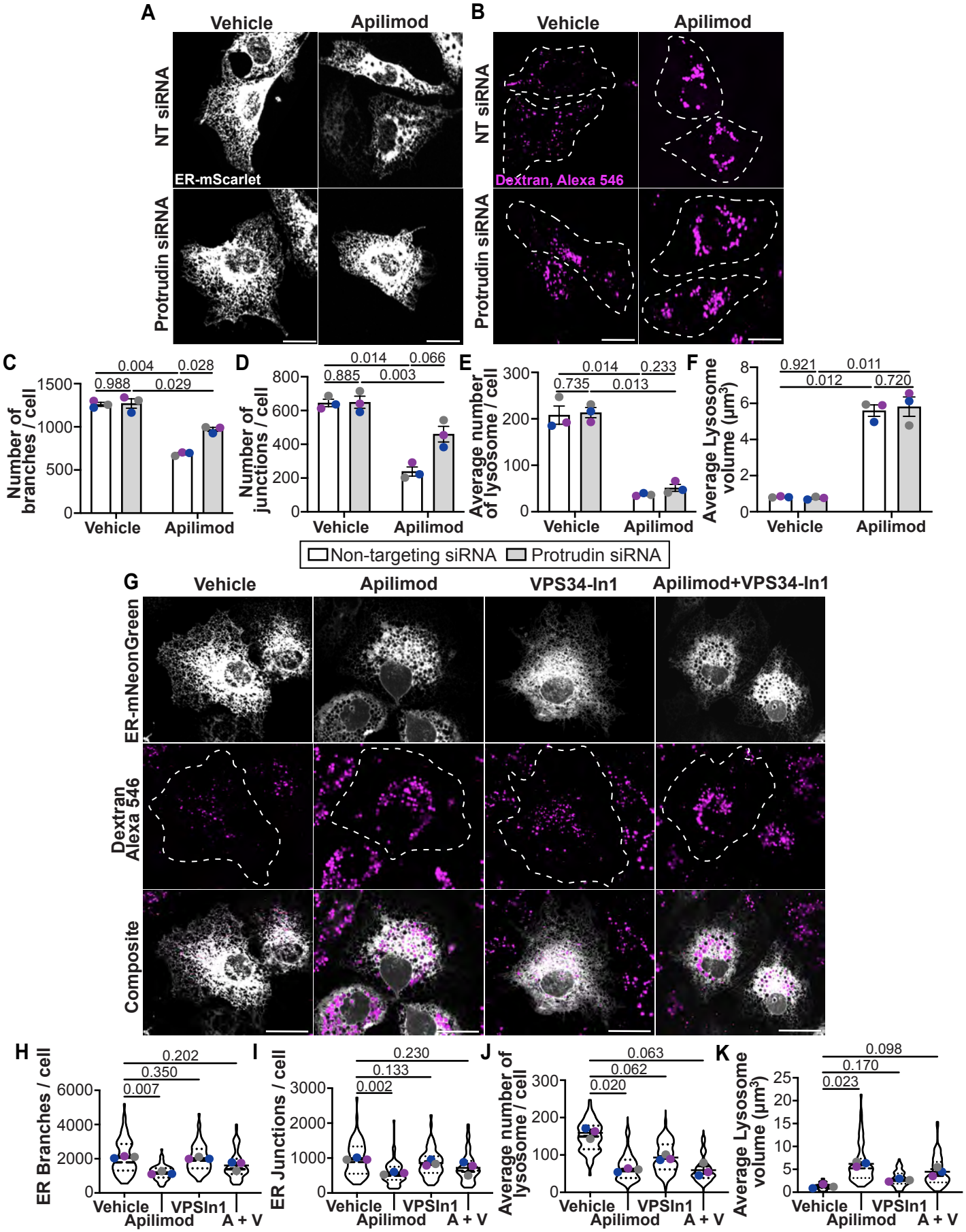
A
Vehicle
Apilimod
NT siRNA
Protrudin siRNA
ER-mScarlet
B
Vehicle
Apilimod
NT siRNA
Protrudin siRNA
Dextran, Alexa 546
C
Number of branches / cell
0.004
0.028
0.988
0.029
Vehicle
Apilimod
D
Number of junctions / cell
0.014
0.066
0.885
0.003
Vehicle
Apilimod
E
Average number of lysosome / cell
0.014
0.233
0.735
0.013
Vehicle
Apilimod
F
Average Lysosome volume (μm³)
0.921
0.011
0.012
0.720
Vehicle
Apilimod
Non-targeting siRNA
Protrudin siRNA
G
Vehicle
Apilimod
VPS34-In1
Apilimod+VPS34-In1
ER-mNeonGreen
Dextran Alexa 546
Composite
H
ER Branches / cell
0.202
0.350
0.007
Vehicle
Apilimod
VPSIn1
A + V
I
ER Junctions / cell
0.230
0.133
0.002
Vehicle
Apilimod
VPSIn1
A + V
J
Average number of lysosome / cell
0.063
0.062
0.020
Vehicle
Apilimod
VPSIn1
A + V
K
Average Lysosome volume (μm³)
0.098
0.170
0.023
Vehicle
Apilimod
VPSIn1
A + V

FIGURE 7.

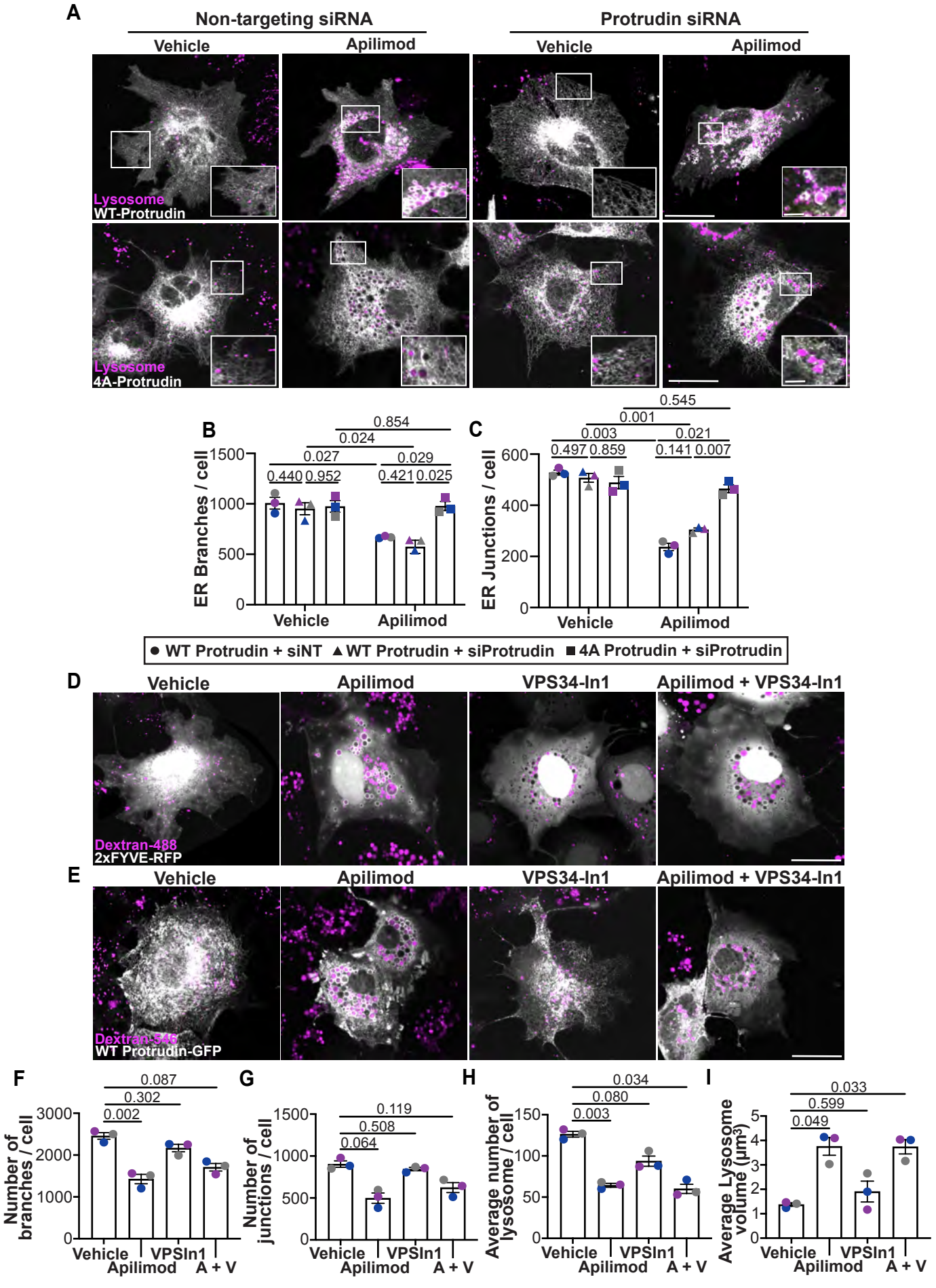
A
Non-targeting siRNA
Protrudin siRNA
Vehicle
Apilimod
Vehicle
Apilimod
Lysosome
WT-Protrudin
Lysosome
4A-Protrudin
B
ER Branches / cell
1500
1000
500
0
0.854
0.024
0.027
0.029
0.440
0.952
0.421
0.025
Vehicle
Apilimod
C
ER Junctions / cell
600
400
200
0
0.545
0.001
0.003
0.021
0.497
0.859
0.141
0.007
Vehicle
Apilimod
WT Protrudin + siNT
WT Protrudin + siProtrudin
4A Protrudin + siProtrudin
D
Vehicle
Apilimod
VPS34-In1
Apilimod + VPS34-In1
Dextran-488
2xFYVE-RFP
E
Vehicle
Apilimod
VPS34-In1
Apilimod + VPS34-In1
Dextran-546
WT Protrudin-GFP
F
Number of branches / cell
3000
2000
1000
0
0.087
0.302
0.002
Vehicle
Apilimod
VPSIn1
A + V
G
Number of junctions / cell
1500
1000
500
0
0.119
0.508
0.064
Vehicle
Apilimod
VPSIn1
A + V
H
Average number of lysosome / cell
150
100
50
0
0.034
0.080
0.003
Vehicle
Apilimod
VPSIn1
A + V
I
Average Lysosome volume (μm³)
5
4
3
2
1
0
0.033
0.599
0.049
Vehicle
Apilimod
VPSIn1
A + V

FIGURE 8.

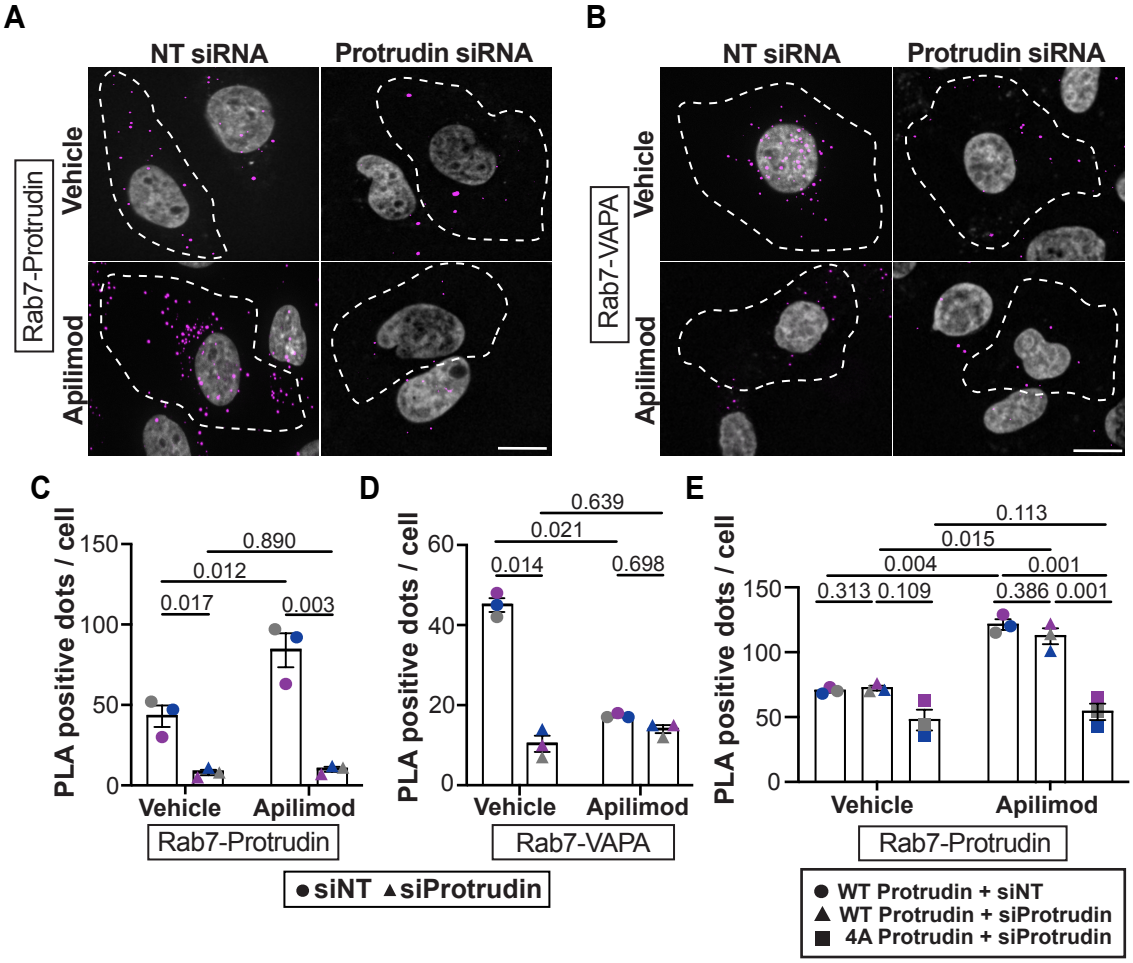
A
NT siRNA
Protrudin siRNA
Rab7-Protrudin
Vehicle
Apilimod
B
NT siRNA
Protrudin siRNA
Rab7-VAPA
Vehicle
Apilimod
C
PLA positive dots / cell
150
100
50
0
0.890
0.012
0.017
0.003
Vehicle
Apilimod
Rab7-Protrudin
D
PLA positive dots / cell
60
40
20
0
0.639
0.021
0.014
0.698
Vehicle
Apilimod
Rab7-VAPA
E
PLA positive dots / cell
150
100
50
0
0.113
0.015
0.004
0.001
0.313
0.109
0.386
0.001
Vehicle
Apilimod
Rab7-Protrudin
●siNT ▲siProtrudin
● WT Protrudin + siNT
▲ WT Protrudin + siProtrudin
■ 4A Protrudin + siProtrudin

FIGURE 9.

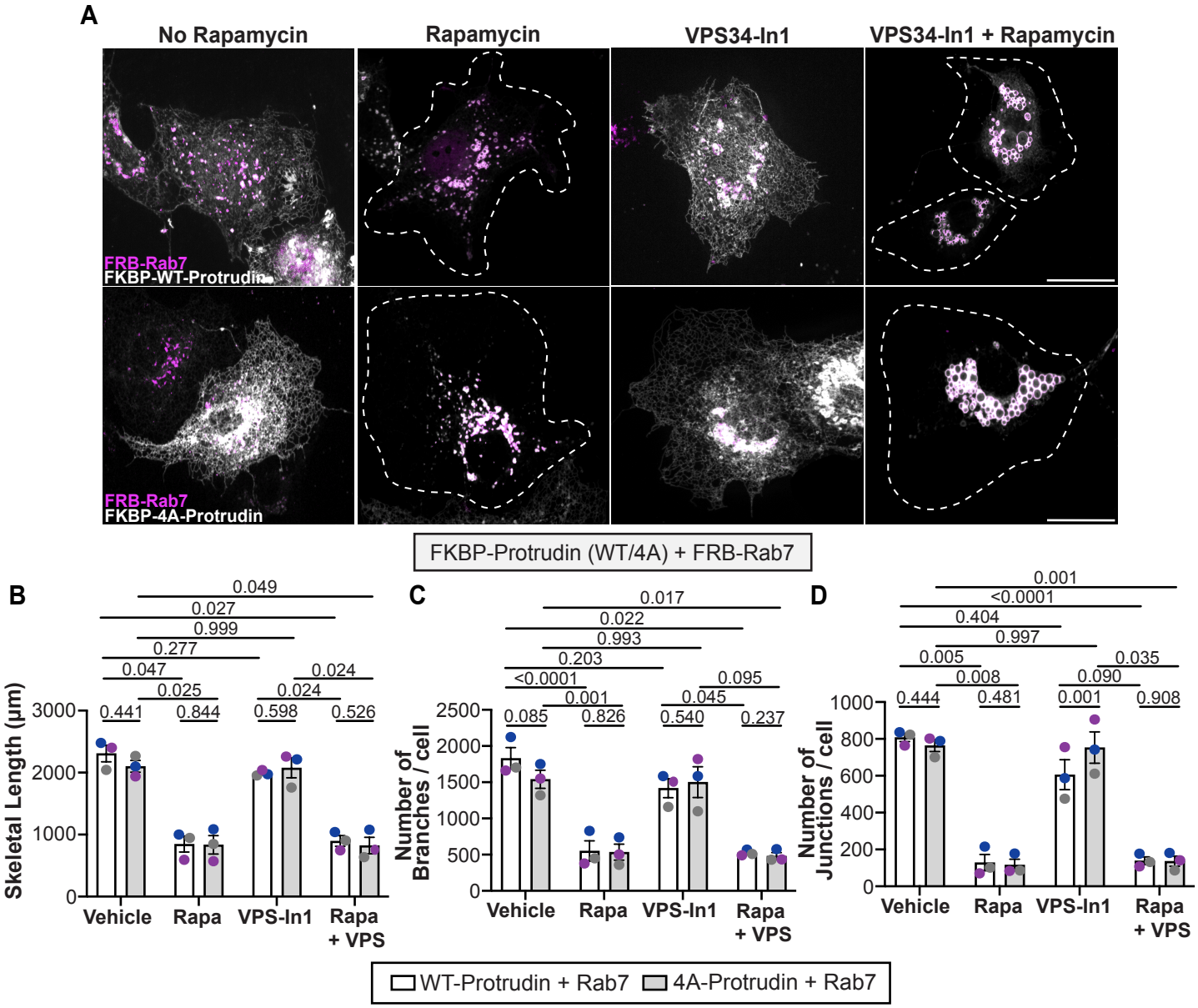
A
No Rapamycin
Rapamycin
VPS34-In1
VPS34-In1 + Rapamycin
FRB-Rab7
FKBP-WT-Protrudin
FRB-Rab7
FKBP-4A-Protrudin
FKBP-Protrudin (WT/4A) + FRB-Rab7
B
Skeletal Length (µm)
0.049
0.027
0.999
0.277
0.047
0.025
0.024
0.024
0.441
0.844
0.598
0.526
Vehicle
Rapa
VPS-In1
Rapa + VPS
C
Number of Branches / cell
0.017
0.022
0.993
0.203
<0.0001
0.001
0.095
0.045
0.085
0.826
0.540
0.237
Vehicle
Rapa
VPS-In1
Rapa + VPS
D
Number of Junctions / cell
0.001
<0.0001
0.404
0.997
0.005
0.008
0.035
0.090
0.444
0.481
0.001
0.908
Vehicle
Rapa
VPS-In1
Rapa + VPS
WT-Protrudin + Rab7
4A-Protrudin + Rab7